Key Points:
- Brittle and plastic deformation in quartz are intimately connected through crack healing processes in the presence of aqueous fluids
- H$_2$O weakening takes place by dislocation generation and multiplication at healed cracks and very small fluid inclusions
- H$_2$O is recycled between fluid inclusions and structurally bound H in dislocations and vice versa

Correspondence to:
H. Stünitz,
holger.stunitz@uit.no

Water redistribution in experimentally deformed natural milky quartz single crystals—Implications for H$_2$O-weakening processes

H. Stünitz[1,2] (iD), A. Thust[3,4], R. Heilbronner[3], H. Behrens[5], R. Kilian[3] (iD), A. Tarantola[6], and J. D. Fitz Gerald[7]

[1]Department of Geosciences, University of Tromsø, Tromsø, Norway, [2]Institut de la Sciences de la Terre d'Orléans, Université d'Orléans, Orléans, France, [3]Department of Geology, Basel University, Basel, Switzerland, [4]Now at Institut für Geowissenschaften, Frankfurt, Germany, [5]Institute for Mineralogy, Leibniz University of Hannover, Hannover, Germany, [6]Université de Lorraine, CNRS, CREGU, GeoRessources, Vandœuvre-lès-Nancy, France, [7]Research School of Earth Sciences, Australian National University, Canberra, A.C.T., Australia

Abstract Natural quartz single crystals were experimentally deformed in two orientations: (1) $\perp$ to one prism plane and (2) in O$^+$ orientation at 900 and 1000°C, 1.0 and 1.5 GPa, and strain rates of ~$1 \times 10^{-6} \, \text{s}^{-1}$. In addition, hydrostatic and annealing experiments were performed. The starting material was milky quartz, which consisted of dry quartz with a large number of fluid inclusions of variable size up to several 100 μm. During pressurization fluid inclusions decrepitated producing much smaller fluid inclusions. Deformation on the sample scale is anisotropic due to dislocation glide on selected slip systems and inhomogeneous due to an inhomogeneous distribution of fluid inclusions. Dislocation glide is accompanied by minor dynamic recovery. Strongly deformed regions show a pointed broad absorption band in the ~3400 cm^{-1} region consisting of a superposition of bands of molecular H$_2$O and three discrete absorption bands (at 3367, 3400, and 3434 cm^{-1}). In addition, there is a discrete absorption band at 3585 cm^{-1}, which only occurs in deformed regions and reduces or disappears after annealing, so that this band appears to be associated with dislocations. H$_2$O weakening in inclusion-bearing natural quartz crystals is assigned to the H$_2$O-assisted dislocation generation and multiplication. Processes in these crystals represent recycling of H$_2$O between fluid inclusions, cracking and crack healing, incorporation of structurally bound H in dislocations, release of H$_2$O from dislocations during recovery, and dislocation generation at very small fluid inclusions. The H$_2$O weakening by this process is of disequilibrium nature because it depends on the amount of H$_2$O available.

1. Introduction

Quartz is one of the most important constituents of the Earth's crust not only in terms of volume proportion but also as a means of determining physical properties. One of the reasons for its importance is the vast amount of data available for quartz so that even if its volume proportion within a given rock type is subordinate, some deformation and other properties of the rock may be inferred from measuring certain parameters of quartz present in the rock (i.e., grain size, H$_2$O and trace element content, and isotopic composition).

Using quartz as a deformation indicator is particularly important for determining the rheology of the crust. While the strength of the upper crust is assumed to be controlled by friction, regardless of rock composition [*Byerlee*, 1968; *Kohlstedt et al.*, 1995], the rheology at temperatures higher than the brittle-plastic transition [*Kohlstedt et al.*, 1995] will be controlled by viscous behavior of individual minerals. For the minerals calcite, quartz, and olivine, there is a reasonably well constrained data base of constitutive equations, which can be used to describe the rheology of the crust and upper mantle. In natural deformation at geological strain rates of ~10^{-12}s^{-1}, the brittle-plastic transition in quartz occurs between ~280 and ~300°C [*Stipp et al.*, 2002a, 2002b], which corresponds to a depth of ~10 km for geothermal gradients of ~30°C km^{-1}.

However, the brittle-plastic transition will depend on the presence of H$_2$O [e.g., *Menegon et al.*, 2011; *Kilian et al.*, 2016] and on the confining pressure, because H$_2$O weakening (and H$_2$O fugacity) is of critical importance for the rheology of quartz: Dry quartz in experiments is extremely strong, whereas "wet" quartz is among the weaker minerals. In order to account for the effect of H$_2$O in the constitutive equations, the physics of the weakening process need to be understood, and that is why this study has been performed.

Since its discovery by *Griggs and Blacic* [1965], H_2O weakening in quartz and other silicates has received a lot of attention. The H_2O weakening in olivine appears to be primarily caused by point defects [e.g., *Mei and Kohlstedt*, 2000a, 2000b; *Zhao et al.*, 2004; *Walker et al.*, 2007], while the mechanisms of the weakening process in quartz and other minerals are still poorly understood [e.g., *Paterson*, 1989]. The original weakening mechanism for quartz ("hydrolytic weakening") introduced by *Griggs* [1967] and reformulated by *Griggs* [1974] proposes a lower bond strength of hydrolyzed Si-O bonds resulting in a lower Peierls stress for the dislocation glide process. In addition, it has been demonstrated that recovery and recrystallization processes are promoted by H_2O and contribute substantially to weakening in quartz [e.g., *Tullis and Yund*, 1989; *Cordier and Doukhan*, 1989]. Thus, there may be multiple processes by which H_2O affects the deformation of quartz [*Kronenberg*, 1994; *Cordier et al.*, 1994], and this situation may apply to other silicates as well. For this reason, a study of H_2O weakening in quartz may be relevant to many silicates which may show similar effects.

H_2O weakening of quartz is associated with molecular forms of H_2O and/or with dissociated forms of H_2O present as a hydrogarnet (4H)Si or other isolated (OH) and/or structurally bound defects [*Doukhan and Trépied*, 1985; *Paterson*, 1989; *Kronenberg*, 1994; *Cordier et al.*, 1994]. Molecular H_2O may form small fluid clusters in synthetic quartz [*Kekulawala et al.*, 1981; *Paterson*, 1986; *McLaren et al.*, 1989] or fluid inclusions in natural quartz. Very small aggregates of H_2O (<1 to a few nm) are referred to as clusters (up to ~200 molecules of H_2O [*Aines et al.*, 1984]). The equilibrium solubility of H_2O in the form of (4H)Si defects is far below 100 $H/10^6$ Si, even at very high temperatures and pressures [*Paterson*, 1986, 1989], and it is likely that such low H_2O contents will represent "dry" and strong quartz for deformation by dislocation creep in experiments. Thus, weakening of quartz requires the infiltration of H_2O or (OH) into the quartz grains if intragranular slip- or climb-related or dislocation multiplication processes are to be activated.

For the infiltration of H_2O or OH, the product of diffusivity and solubility is important. The infiltration will be limited by the solubility to increase the H_2O content inside grains. It has been shown that, although diffusivity of H_2O through quartz is relatively high [*Cordier et al.*, 1988; *Farver and Yund*, 1991], the solubility (equilibrium storage capacity) for H_2O in quartz is so small that diffusive infiltration of H_2O into quartz grains is effectively impossible at laboratory time scales [*Kronenberg et al.*, 1986; *Rovetta et al.*, 1986; *Gerretsen et al.*, 1989]. The observed H_2O infiltration into quartz in experiments has taken place through microcracks and not by diffusion [*Kronenberg et al.*, 1986; *Gerretsen et al.*, 1989].

In experiments, the degree of mechanical weakening increases with increasing H_2O content of single and polycrystalline samples [*Griggs*, 1967; *Blacic and Christie*, 1984; *Cordier and Doukhan*, 1989; *Hirth and Tullis*, 1992; *den Brok et al.*, 1994; *Kronenberg et al.*, 2001]. Single crystal samples deformed in the semibrittle field (at a given temperature and strain rate [*Evans and Kohlstedt*, 1995]) have been considered as "dry" in the early experiments of *Griggs and Blacic* [1965] and have a H_2O content of 140 and 60 $H/10^6$ Si. *Poirier* [1985] considers quartz "dry" and brittle at 1300°C at H_2O contents of <80 $H/10^6$ Si, whereas the weak and wet synthetic crystals contain several hundreds [*Muto et al.*, 2011] or >1000 $H/10^6$ Si [*Griggs*, 1967] before deformation. Thus, absence of brittle deformation and fully crystal plastic deformation occurs probably at H_2O contents of more than a few hundred $H/10^6$Si [*Kronenberg*, 1994] or ~500 $H/10^6$ Si [*Poirier*, 1985] at laboratory strain rates and temperatures, whereas crystals with H_2O contents lower than ~150 $H/10^6$ Si deform by semibrittle or even brittle deformation mechanisms in the laboratory.

Natural quartz single crystals may contain a large amount of H_2O in the form of fluid inclusions (milky quartz) and are weak in experiments. However, it has been noticed from the beginning of experimental work that the distribution of strain is inhomogeneous in natural quartz [*Griggs*, 1967; *Blacic*, 1975]. The problem was avoided by using synthetic crystals with a known and homogeneous H_2O content (on the sample scale) in most subsequent experiments [*Blacic*, 1975; *Kirby*, 1975; *Morrison-Smith et al.*, 1976; *Kekulawala et al.*, 1981; *Linker and Kirby*, 1981; *Doukhan and Trépied*, 1985; *Cordier and Doukhan*, 1989; *Cordier et al.*, 1994; *Muto et al.*, 2011]. *Morrison-Smith et al.* [1976] have observed high dislocation densities and tangles in association with H_2O clusters or minute fluid inclusions in synthetic quartz crystals. Later it has been shown that dislocation nucleation and multiplication in the synthetic crystals is induced by these in-grown clusters of H_2O [*McLaren et al.*, 1983, 1989; *Cordier and Doukhan*, 1989].

So far, all observed effects of H_2O weakening in synthetic crystals can be explained by the H_2O-cluster-induced dislocation nucleation and multiplication without a necessary reduction of Peierls stress for

dislocation glide [*McLaren et al.*, 1989], although it does not exclude that H_2O or OH may have an effect on the resistance to glide. Thus, from the study of *McLaren et al.* [1989], it is concluded that synthetic crystals probably do not represent the typical situation of quartz weakening as it may occur in nature, because the high number of grown-in H_2O clusters, which cause the weakening in synthetic crystals, are not necessarily common in natural crystals.

Most of the published earlier experimentally deformed microstructures of the natural and synthetic single crystals show cracks in addition to crystal plastic deformation features [e.g., *Blacic*, 1975; *Morrison-Smith et al.,* 1976]. In a careful microstructural investigation of experimentally deformed natural quartz crystals *Fitz Gerald et al.* [1991] have demonstrated that cracking and crack healing are very important processes for the generation and multiplication of dislocations in otherwise very low dislocation density crystals. The processes take place during early stages of the experiments, and in such samples, crystal plastic deformation and dislocation densities are directly related to porosity and healed cracks [*Fitz Gerald et al.*, 1991]. Cracking and subsequent crack healing are also important for the nucleation of new grains (recrystallization) as shown in experiments by *den Brok and Spiers* [1991], *Vernooij et al.* [2006], *Trepmann et al.* [2007], and *Trepmann and Stöckhert* [2013]. One aspect, which has not been investigated systematically, is the H_2O speciation in the defects induced by microcracking and subsequent dislocation glide deformation.

The weakening effect in natural quartz is pressure dependent so that flow stress in dislocation creep decreases with increasing confining pressure [*Heard and Carter*, 1968; *Tullis et al.,* 1979; *Mainprice and Paterson*, 1984; *Kronenberg and Tullis*, 1984; *Post et al.*, 1996; *Holyoke and Kronenberg*, 2013]. The pressure dependence of the weakening process is taken into account by introducing a fugacity term to the onstitutive relationships for quartz, as it is done for olivine [*Kohlstedt et al.*, 1995; *Post et al.*, 1996; *Hirth et al.*, 2001; *Chernak et al.,* 2009; *Holyoke and Kronenberg*, 2013]. The synthetic crystals do not show this dependence, because the dislocation nucleation process appears to take place at low and high confining pressures alike [*McLaren et al.*, 1989]. This marks another difference between natural and synthetic quartz material.

From the fact that wet quartz is weak in experiments, it has been inferred that H_2O weakening takes place in the deformation of natural quartz, too, because quartz is one of the weaker minerals in naturally deformed crustal rocks, even at temperatures of low metamorphic grade. Thus, the process of H_2O weakening in natural quartz crystals remains an important research topic, and the questions of H_2O infiltration, speciation, and weakening mechanisms need to be addressed. From the short literature review of some pertinent aspects of quartz deformation given above, it can be seen that such a study has to use a natural quartz material, and it should be carried out on single crystals in order to study the effects of dislocation nucleation, multiplication, and/or climb/recovery features without additional effects of H_2O along grain boundaries. In addition, milky quartz crystals are most suited for such studies, because they contain sufficient amounts of H_2O to induce weakening, and H_2O transport into the crystals from an external source is not required. Such a study has to be carried out in a solid medium deformation apparatus to obtain the confining pressures required for the experimental deformation of natural quartz crystals.

This study will focus on the characterization of the content, distribution, and especially the speciation of H_2O/OH before and after deformation of milky quartz crystals. In addition, interaction of H_2O with dislocations, its speciation, and possible effects for H_2O weakening and the involved processes are studied.

2. Materials and Methods

2.1. Deformation Experiments

Axial compression experiments were performed in a modified solid medium (NaCl) Griggs apparatus [*Griggs*, 1967; *Tullis and Tullis*, 1986] at the Department of Geology of the University of Tromsø. The cylindrical samples (6.45—6.48 mm in diameter and 10 to 13 mm in length) were cored from a milky single crystal. The sample ends were ground plane parallel (within 1 to 2 μm) and normal to the cylinder axis.

Two different sample orientations were prepared for deformation experiments (Figure 1): (1) One orientation with the highest principal stress (σ_1) normal to one of the prism planes (⊥m orientation), (2) one orientation with σ_1 inclined 45° to [*c*] and 45° to $< a >$ (O^+ orientation). These orientations were chosen to activate
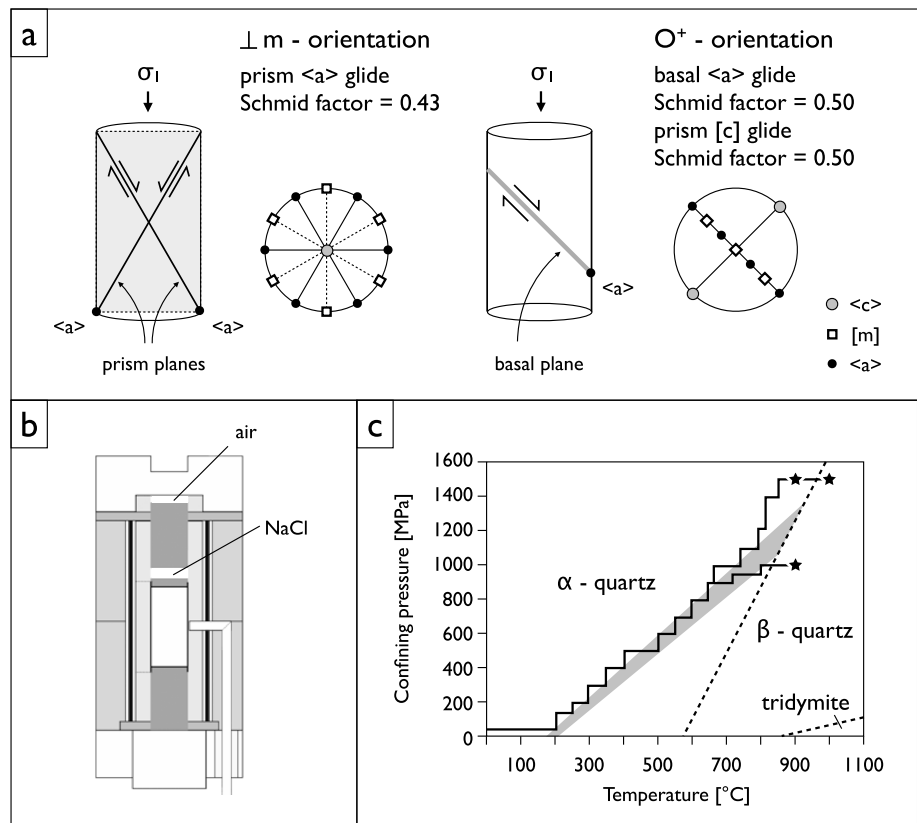
Figure 1. Experimental setup. (a) Schematic drawing and stereographic plot of the ⊥m and O$^+$ orientation of quartz single crystals used in experiments. Schmid factors are indicated (prism [c] slip is on {−2110}). (b) Sample assembly used in the solid medium deformation apparatus (modified after *Tarantola et al.* [2010]), additional salt disc and gap in top Pb piece are highlighted. (c) *P-T* path to experimental conditions. Isochores (enclosing grey region in α-quartz) were obtained from fluid inclusions of the starting material. Stars represent conditions at the start of the deformation experiments. Solid stepped lines show different *P-T* paths for attaining the experimental conditions. The stability fields of α-, β-quartz and tridymite are separated by stippled lines.

different slip systems: In orientation (1), Prism $<a>$ slip on two prism planes {10-10} with Schmid factor of 0.43; in orientation (2): Basal (0001) $<a>$ slip (Schmid factor 0.5) and prism [c] slip (Schmid factor 0.50); and some rhomb and prism $<a>$ slip with Schmid factors of 0.42 and lower; Figure 1).

The quartz cylinders have been encapsulated in a Pt jacket (0.15 mm wall thickness) and welded at the ends in a can-like manner. Al$_2$O$_3$ cylinders of 6.35 mm diameter were used as piston material. In some experiments, an additional NaCl disc was placed between two upper Al$_2$O$_3$ pistons to protect the sample from cracking while attaining of experimental conditions (Figure 1c) [cf. *Tarantola et al.* [2010]]. This method is successful if the pressure is increased slowly. Heating of the sample was achieved with a graphite resistance furnace stabilized by two soft-fired pyrophyllite sleeves. There is an estimated maximum temperature difference of up to 10% between the central thermocouple position and the lower end of the upper alumina piston [*Pec et al.*, 2016].

The samples were deformed at temperatures of 900°C and 1000°C and confining pressures of 1.0 and 1.5 GPa. Most of the experiments were carried out in the α-quartz stability field (Figure 1c; 900°C, 1.5 GPa), some in the β-quartz stability field (Figure 1c; 900°C, 1.0 GPa, 1000°C, and 1.5 GPa). The phase transformation causes decrepitation of fluid inclusions [*Doppler and Bakker*, 2014]. The axial strain rate ranged between $1.2*10^{-6}$ and $8.5*10^{-7}\,s^{-1}$ and the finite shortening between 3.9 and 32.4%. Strength was determined using an external load cell with an estimated error of ± 30 MPa for the sample [*Holyoke and Kronenberg*, 2010]. The correction for the mechanical data proposed by *Holyoke and Kronenberg* [2010] is included, together with all other experimental conditions, in Table 1.

Table 1. Experimental Conditions for All Experiments at 900°C and 1000°C (Pressurized Only, Deformed, and Annealed)

Sample Number/Orientation	P_{conf} (MPa)	T (°C)	Sample Strain (%)	Peak Stress (MPa)	Peak Stress Corrected* (MPa)	Strain Rate (s^{-1})	Notes
143 ATH/⊥m	1500	900					at *P-T*/undeformed
151 ATH/⊥m	250	250					at *P-T*/undeformed
157 ATH/⊥m	630	500					at *P-T*/undeformed
168 ATH/⊥m	1100	750					at *P-T*/undeformed
170 ATH/⊥m	1000	880					at *P-T*/undeformed
171 ATH/ O+	1017	800					at *P-T*/undeformed
201 ATH/ O+	620	550					at *P-T*/undeformed
230 ATH/⊥m	650	750					at *P-T*/undeformed
196 ATH/⊥m	1480	900					at *P-T*/undeformed
144 ATH/⊥m	1000	900	4.9	149	61	$8.2 * 10^{-7}$	
146 ATH/⊥m	1000	900	16.4	163	71	$8.5 * 10^{-7}$	
152 ATH/⊥m	1000	900	14.7	144	57	$3.99 * 10^{-6}$	
181 ATH/⊥m	1464	900	13.1	416	256	$1.44 * 10^{-6}$	
182 ATH/ O+	1022	900	12	233	122	$1.6 * 10^{-6}$	
184 ATH/ O+	1500	900	4.1	91	18	$1.27 * 10^{-6}$	
187ATH/⊥m	1500	900	minimum 6.2	minimum 130	47		no well-defined HP
190 ATH/⊥m	1500	900	17.9	166	73	$1.61 * 10^{-6}$	
192 ATH/ O+	1466	900	20.1	253	137	$1.55 * 10^{-6}$	
199 ATH/⊥m	1000	900	11.3	222	114	$1.81 * 10^{-6}$	annealed 47 h
203 ATH/ O+	1000	900	5.2	209	105	$1.57 * 10^{-6}$	
205 ATH/ O+	1000	900	5.3	159	68	$1.19 * 10^{-6}$	
207 ATH/⊥m	1500	900	9.6	150	61	$1.28 * 10^{-6}$	
238 ATH/⊥m	1450	1000	15.3	133	49	$1.93 * 10^{-6}$	
241 ATH/ O+	1480	1000	12.5	136	51	$1.95 * 10^{-6}$	
244 ATH/ O+	1016	900	8.6	299	170	$1.78 * 10^{-6}$	annealed 48 h
246 ATH/ O+	1500	900	7.6	188	89	$1.35 * 10^{-6}$	
252 ATH/⊥m	1500	1000	32.4	176	80	$2.13 * 10^{-6}$	

*Stress correction according to *Holyoke and Kronenberg* [2010].

Two experiments (one for each orientation) were deformed to ~10% strain and subsequently annealed for about 48 h after deformation and then quenched. Before the annealing the differential stress was lowered to hydrostatic conditions.

2.2. Orientation Imaging

Thin sections were prepared for texture and microstructure analysis. The computer integrated microscopy method [see *Heilbronner and Barrett*, 2013] was used to obtain *c* axis orientation and misorientation images. The software Image SXM was used to measure the size distribution of fluid inclusions.

2.3. Microthermometry

Microthermometry and Raman microspectroscopy were carried out in the Fluid Inclusion Laboratory of the Institute of Geological Sciences, University of Bern. A Linkam™ THMSG 600 heating-cooling stage was applied; calibrated using the following phase transitions in synthetic fluid inclusions in quartz: the triple point of CO_2 at −56.6°C, the triple point of H_2O at 0.0°C, and the critical point of H_2O at 374.0°C. The stage was mounted on an Olympus™ BX51 microscope equipped with 40X and 100X objectives. About 180 fluid inclusions were randomly selected to represent the range in shape, size, and distance to the sample surface. For each inclusion, T_e, the eutectic temperature of the aqueous phase, $T_{m(ice)}$, the final ice melting temperature, $T_{m(cla)}$, the final clathrate dissociation temperature, and $T_{h(tot)}$, the total homogenization temperature, were checked and measured whenever observed. The vapor phases of individual inclusions were analyzed for H_2, N_2, CH_4, and CO_2 at room temperature using a Jobin-Yvon™ LabRAM HR800 laser-Raman spectrometer.

2.4. Fourier Transform Infrared Spectroscopy

The water content and OH speciation were analyzed by Fourier transform infrared (FTIR) spectroscopy in different samples representing the material before deformation, after pressurization (no axial deformation), and after deformation. The system used at the University of Hannover (Germany) is an IR microscope
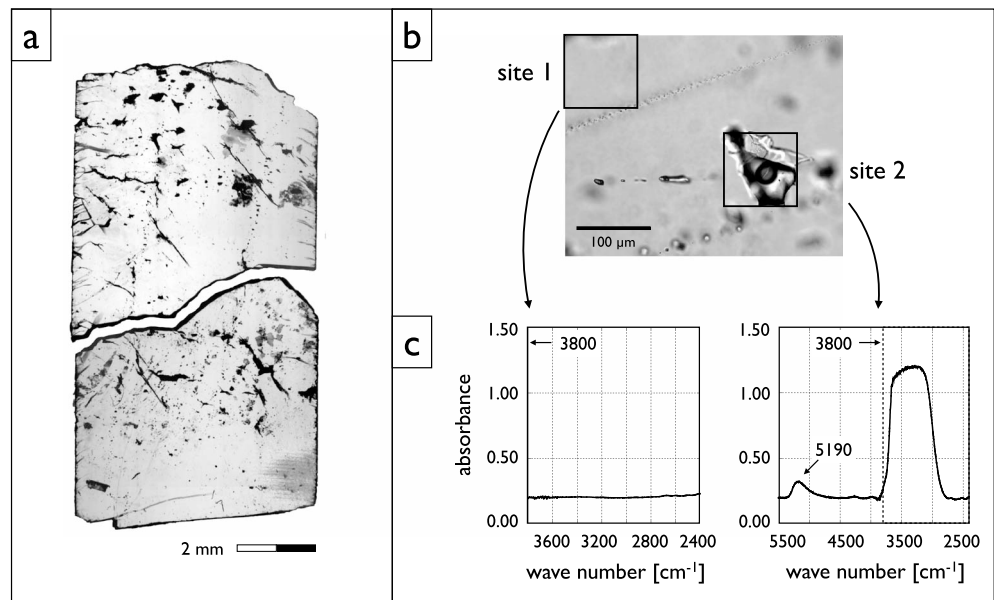
Figure 2. Fluid inclusions in the starting material. (a) Thick section of a sample with heterogeneous distribution of fluid inclusions, small cracks emanating from the vertical edges result from drilling of the core. (b) Thin section micrograph of dry quartz matrix with fluid inclusions. Two sites of FTIR measurements are indicated by frames. (c) FTIR absorption spectra for dry quartz with nearly no absorbance (site 1) and for fluid inclusion (site 2) showing oversaturation between 3000 and 3600 cm^{-1} and a peak at 5190 cm^{-1} typical for molecular water. Note the different wave number range of spectra.

IRscope II attached to a Bruker IFS88 FTIR spectrometer. Measurements were carried out on doubly polished sections cut parallel to the cylinder axis with a thickness between 120 μm and 500 μm. Spectra with nonpolarized light at room temperatures were used to quantify the water content in the crystals. Some additional spectra were recorded using a cooling stage (cooled by liquid nitrogen) down to ~ –150°C. Some spectra were obtained using polarized light. Point measurements with a spot size of 100 × 100 μm were recorded over a wave number range from 500 to 5000 cm^{-1} by using 50 scans per spectrum with a spectral resolution of 2 cm^{-1}. Background spectra were collected for each sample at the beginning of and several times during the measurements and subtracted from every single spectrum.

Water concentration calculations are based on the wavelength-dependent, integral molar absorption coefficient by *Paterson* [1982] for wave numbers from 3780 cm^{-1} to 3000 cm^{-1}. The link between FTIR absorption and water concentration is given by the Beer-Lambert law, $A_i = c \cdot t \cdot \epsilon_i$, where c is the concentration, t is the thickness, and ϵ_i is the integral molar absorption coefficient $\epsilon_i = 1/3 \cdot [150 \cdot (3780 \, \text{cm}^{-1} - v \, \text{cm}^{-1})]$, where v is the wave number and the factor of 1/3 refers to *Paterson's* [1982] orientation factor for uniaxial crystals. The water concentration in mol H/l is calculated by $c = \int K(v)/(150 * 1/3(3780 - v)) dv$ where $K(v)$ is the absorption coefficient in cm^{-1} at wave number v. Mole H/l are converted to H/10^{6}Si (or molar ppm H) using the factor 22,600 [*Paterson*, 1982]. A factor of 6.67 may be used to convert from H/Si to weight ppm H$_2$O.

2.5. TEM

Selected regions of deformed crystals were prepared for transmission electron microscopy (TEM) analysis by gluing copper grids (3 mm diameter) to thin sections fastened with thermal glue. The grids and sample material were removed from the glass slide and ion milled. The TEM analysis was carried out on a Phillips 430 TEM at 300 kV acceleration voltage at the Research School of Earth Sciences of the Australian National University in Canberra.

3. Results

3.1. Characterization of the Starting Material

The quartz single crystal used in the experiments is ~60 cm long and has been obtained from an alpine cleft in Switzerland (Planggenstock, Aar Massiv). The large size of the crystal allowed the recovery of several
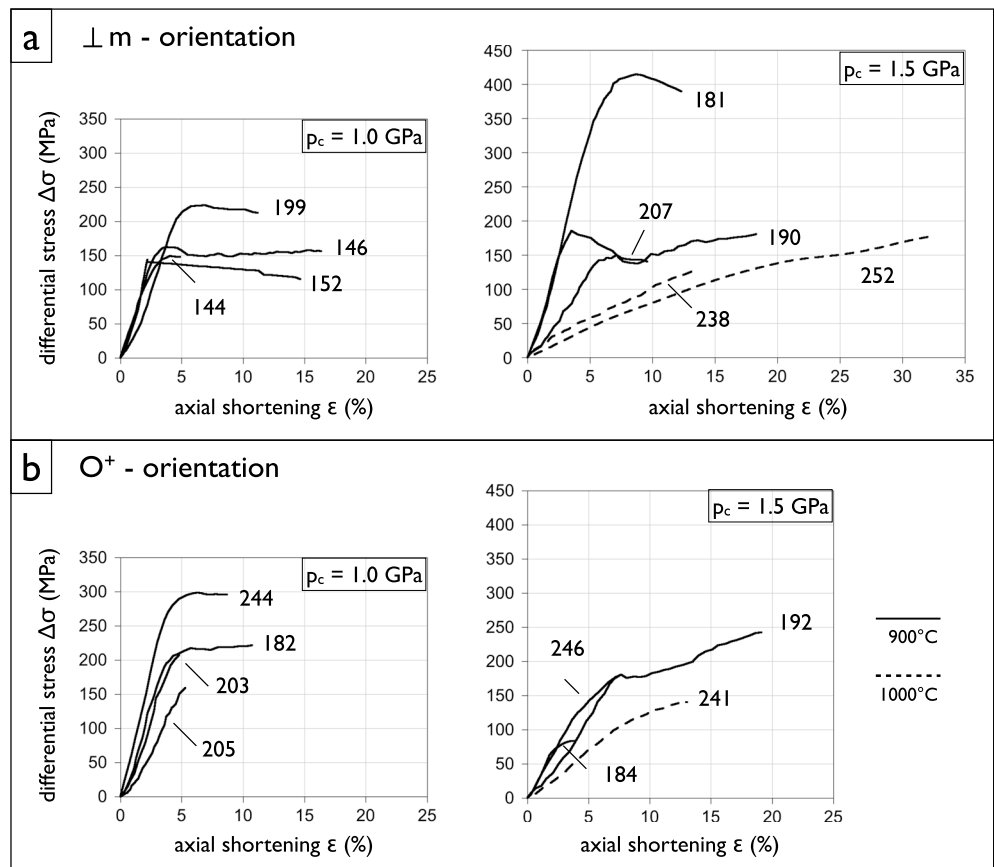
Figure 3. Mechanical data for deformation of quartz single crystals. Differential stress versus axial strain for two different confining pressures (1.0 GPa and 1.5 GPa). Temperature = 900°C (full lines) and 1000°C (dashed lines); strain rate ≈ 10^{-6} s^{-1}. (a) Curves for samples in ⊥m orientation. (b) Curves for samples in O$^+$ orientation.

centimeter-sized layers of fairly constant "milkyness" (i.e., abundance and size of fluid inclusions). One such layer supplied material for ~30 experiments.

Contrary to what was expected initially, the fluid inclusion distribution in the starting material is not homogeneous on the microscopic scale. There is a large variation in size of the fluid inclusions (from < 5 µm to 200 µm, rarely up to 500 µm) and in shape (from equant and regular to highly irregular and flat morphologies), and some inclusion-free regions of up to millimeter size exist.

Clear regions of the quartz crystal situated immediately adjacent to fluid inclusions typically contain amounts of water ~50–150 H/10^{6}Si (Figure 2c) at the given aperture size and sample thickness. Thus, the samples consist of a two-phase starting material of "dry" clear quartz containing water-rich fluid inclusions (Figure 2).

Microthermometric, Raman microspectroscopic, and laser-ablation-ICPMS analyses yield an average composition (in mole percent) of the inclusions of approximately 96.1% H$_2$O, 2.7% NaCl, 0.4% KCl, 0.3% CaCl$_2$, 0.01% LiCl, and 0.3% CO$_2$ [*Tarantola et al.,* 2012]. The isochores from fluid inclusions define a narrow band (Figure 1c) in the pressure-temperature (*P, T*) diagram [cf. *Tarantola et al.,* 2012]. The stepped paths of pressurization and heating follow the isochores of the starting material inclusions as closely as possible, except (1) at the beginning of the experiment, where it has been demonstrated by *Tarantola et al.* [2010] that confining pressure should be higher than the fluid inclusion pressure in order to avoid decrepitation, and (2) at the end of the pressurizing path in order to reach the final pressure and temperature (P, T) conditions (Figure 1c). Deviations of experimental *P, T* conditions from this band are likely to cause the original inclusions to leak, decrepitate, or adapt their molar volume to the imposed *P, T* conditions [e.g., *Sterner et al.,* 1995; *Bodnar,* 2003].
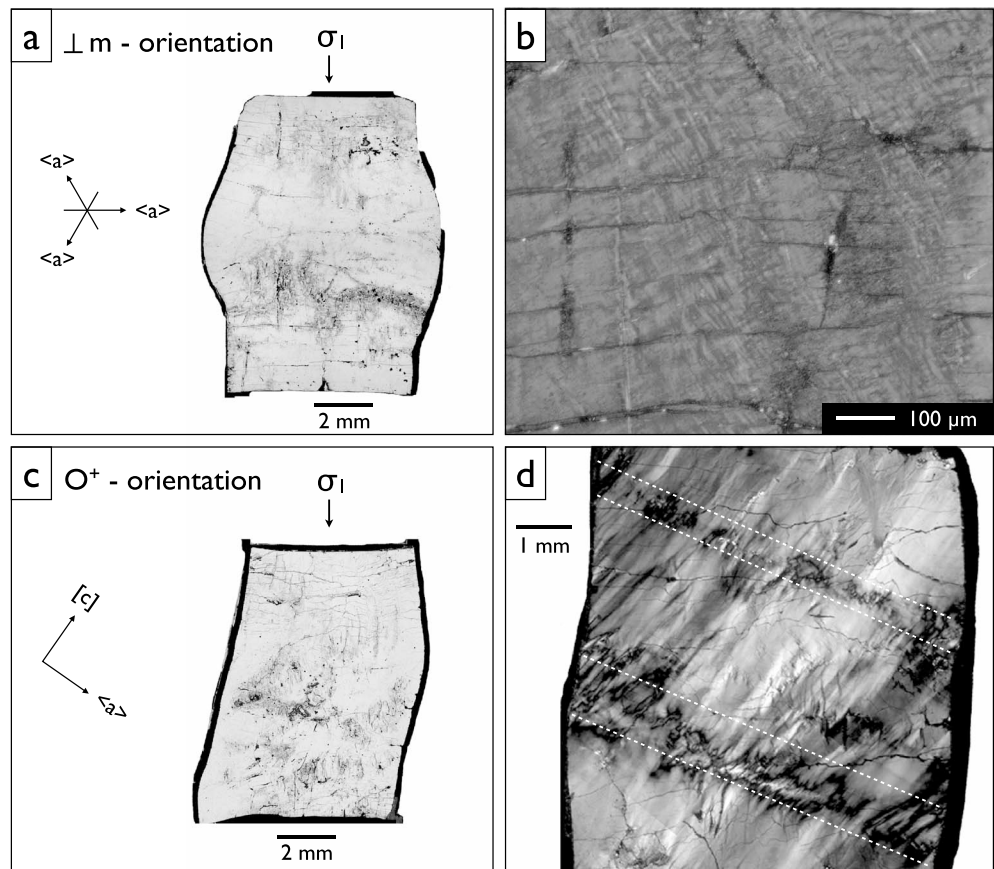
Figure 4. Microstructure of deformed samples. (a, c) Samples are shown in plane polarized light and (b, d) cross-polarized light (right), ⊥m orientation (Figures 4a and 4b) and O$^+$ orientation (Figures 4c and 4d); polarizers are oriented subparallel to [c] axis. (Figure 4a) Sample 146 ATH: typical barrel shape; dusty gray regions contain many fluid inclusions; and horizontal cracks result from unloading. (Figure 4b) Sample 181 ATH: center of sample showing conjugate deformation bands subparallel to $<a>$ axes. (Figure 4c) Sample 192 ATH: typical kinked shape and heterogeneous fluid inclusion distribution. (Figure 4d) Sample 182 ATH: deformation bands (marked by dashed lines) subparallel to trace of basal plane and short wavelength undulatory extinction bands (SWUE) subparallel to the trace of the [c] axis.

3.2. Mechanical Data

The peak strength for most samples ranges between 130 and 230 MPa at 900°C for both orientations (Figure 3). These low values, well below the Goetze criterion (which is the condition $\Delta\sigma = P_{conf}$, where it is empiricially shown that at or above these differential stresses rocks deform in a brittle manner [*Kohlstedt et al.*, 1995]), clearly indicate dominant nonbrittle deformation at the given confining pressures. Samples were deformed to different strains: low-strain experiments to ~5% axial shortening and high-strain experiments to more than 10% axial shortening (Figure 3). The variation in strength of samples is connected with an inhomogeneous strain distribution in the different samples (Figure 4): O$^+$ samples tend to deform in shear or deformation bands, and ⊥m samples tend to bulge in the hottest part of the sample. Thus, the strength variation of samples between O$^+$ and ⊥m orientation at 900°C appears to be caused by strain partitioning.

One sample is clearly stronger than the rest: 181 ATH (Table 1 and Figure 3). In this case the larger parts of the sample contains very few fluid inclusions and has remained almost undeformed so that the strain rate in the deformed parts of the samples is higher by at least a factor of 2 due to strain partitioning.

The expected lower strength at 1.5 GPa compared to 1.0 GPa [cf. *Kronenberg and Tullis*, 1984; *Holyoke and Kronenberg*, 2013] has not been observed (Figure 3). Even if the two samples 181 ATH and 244 ATH are not considered because of their inhomogeneous fluid inclusion distribution, the variation in strengths between individual samples at the same confining pressure (Figure 3) is greater than the difference between samples
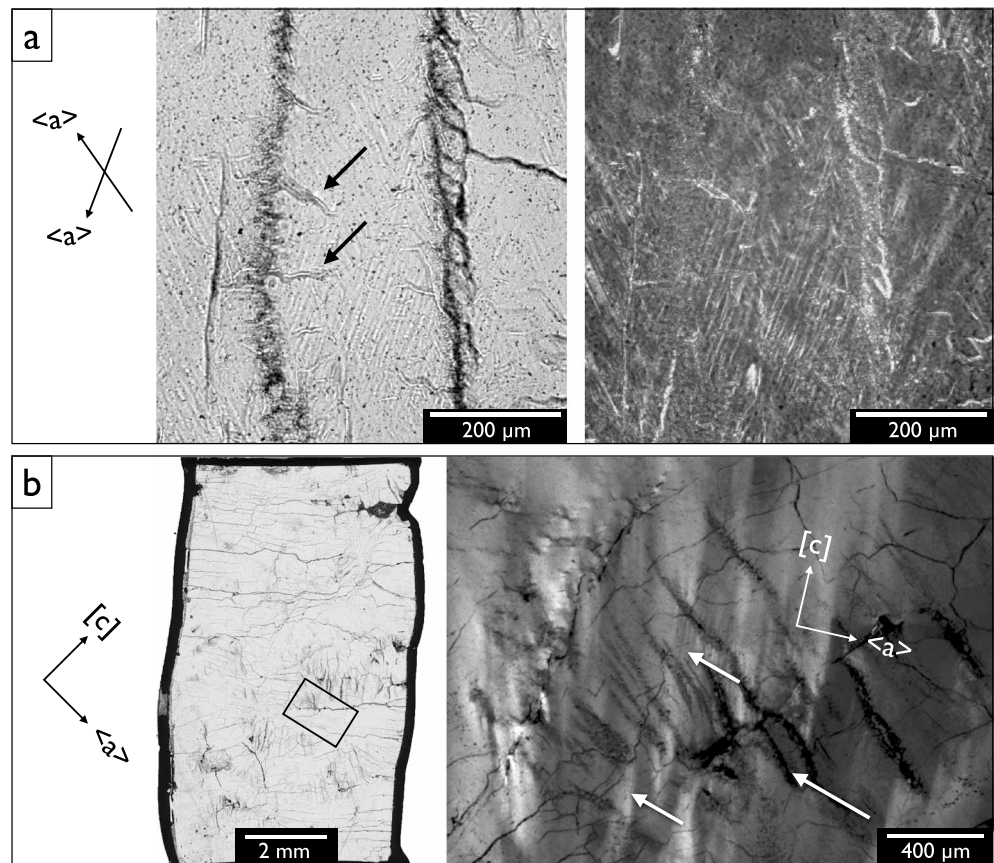
Figure 5. Details of microstructures. (left) Plane polarized light and (right) crossed polarized light. (a) Deformation bands subparallel to the trace of {*m*} between fluid inclusion trails (sample 144 ATH, ⊥m orientation). Unloading cracks (arrows) result from plastic deformation next to the mode 1 cracks. (b) Misorientation zones subparallel to the trace of [*c*] originating at fluid inclusion trails (arrows); frame shows rotated detail on right, (sample 184 ATH; O$^+$ orientation).

at different confining pressures and greater than the expected increase in strength for quartz single crystals due to decreased H_2O fugacity [*Holyoke and Kronenberg*, 2013].

3.3. Sample Deformation

The samples deform mainly by dislocation glide, which is apparent from the sample shape change and the microstructures. The ⊥m samples typically deform in the central region (Figure 4a) where the thermocouple is located (the highest-temperature region of the crystal during the experiment). The sample bulge occurs normal to the axial shortening direction and normal to the [*c*] axis, whereas there is no measurable length change along the [*c*] axis, indicating that two prism $<a>$ slip systems favorably oriented for slip have been activated. The sample end regions often remain undeformed (Figure 4a). In O$^+$ orientation the sample typically shows a kinked geometry (Figures 4c–4d) due to the asymmetric geometry of slip and the lateral displacement at the top and bottom ends of the sample, which have slipped at the piston interfaces (Figure 4c).

The fact that deformation always tends to be localized in the hottest parts of the samples points to temperature dependence of glide or the operation of some recovery processes, e.g., climb of dislocations. However, recrystallization and formation of new grains with discrete high-angle boundaries are observed very rarely in both sample orientations at the relatively low finite sample strain (up to 20%).

If present, recrystallized grains almost exclusively occur along larger cracks. By far, most of the misorientation in the samples occurs with small angles and in the form of diffuse or discrete misorientation bands or zones (see below). In 1000°C experiments, recrystallization is slightly more abundant than at 900°C. The deformation in 1000°C experiments is more homogeneous than at 900°C.
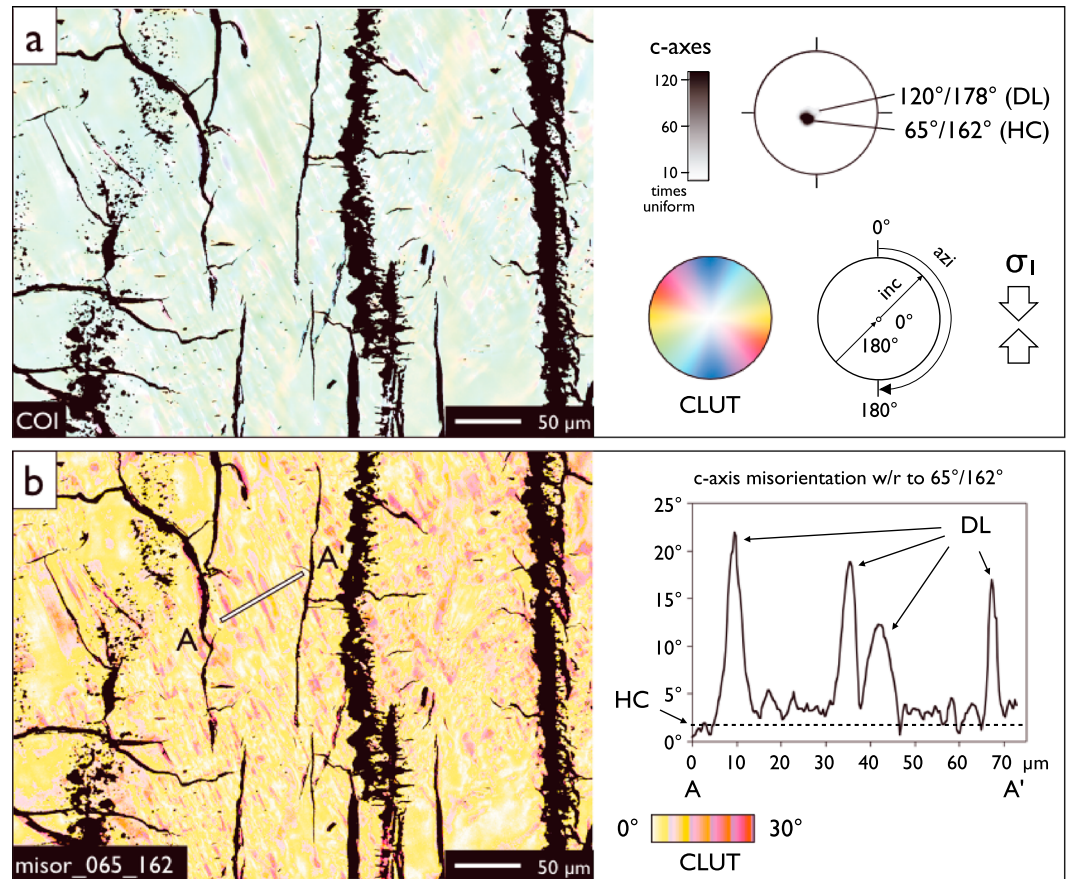
Figure 6. Analysis of *c* axis orientation in deformation lamellae. Sample 144 ATH ⊥m orientation. (a) *c* axis orientation image (COI). On the right, *c* axis pole figure and color look-up table (CLUT) for COI; preferred *c* axis orientations of host crystal (HC) and deformation lamellae (DL) are indicated. Shortening direction applies to Figures 6a and 6b. (b) Misorientation image (misor_065_162) showing angular difference of *c* axis with respect to reference direction 65°/162°. On the right: misorientation profile across deformation lamellae (DL) along trace A-A' shown in image; below CLUT used for color coding.

The small-scale deformation features are more localized in planar zones in the O$^+$ samples compared to ⊥m (Figures 4b and 4d). In both sample orientations deformation lamellae [*Christie et al.,* 1964; *McLaren et al.,* 1970] are present (Figures 5a and 5b). They often are located between fluid inclusion trails, cracks, and en-echelon arrays of fluid inclusions (Figure 5a).

In O$^+$ samples, *c* axis misorientation bands subparallel to the prism planes (or *c* axis) are observed (Figure 5b). The bands are rather diffuse and have a width of up to 200–300 μm. In ⊥m samples, prism $<a>$ glide is dominant and no [*c*] axis reorientation is expected from pure edge dislocation arrays [*Trépied et al.,* 1980]. However, orientation imaging shows [*c*] axis misorientations, which are strongly localized and occur in narrow bands with a small periodicity (Figure 6). The periodic misorientation is observed as small-wavelength undulatory extinction (SWUE) [*Trepmann and Stöckhert,* 2013]. These bands do not display an increasing degree of misorientation over a certain region but a periodic variation of the *c* axis orientation within ~5° over distances of 5–10 μm (Figure 6). The misorientation bands are often associated with prismatic deformation lamellae [*Christie et al.,* 1964; *McLaren et al.,* 1970; *Christie and Ardell,* 1974; *Drury,* 1991], but they extend well beyond the volume of the lamellae (Figure 6). The highest degree of misorientation (up to 20°; Figure 6b) typically occurs in deformation lamellae between trails of fluid inclusions, which decorate cracks parallel to the shortening direction (Figures 5a and 6). The boundaries of misorientation bands appear to be traces of *m* or *a* planes (Figures 5 and 6) [cf. *Trepmann and Stöckhert,* 2013].

In O$^+$ orientation, there are deformed zones subparallel to the basal plane, especially in low-strain samples (Figures 4d and 5c). These zones become indistinct with increasing sample strain, and inside these zones,
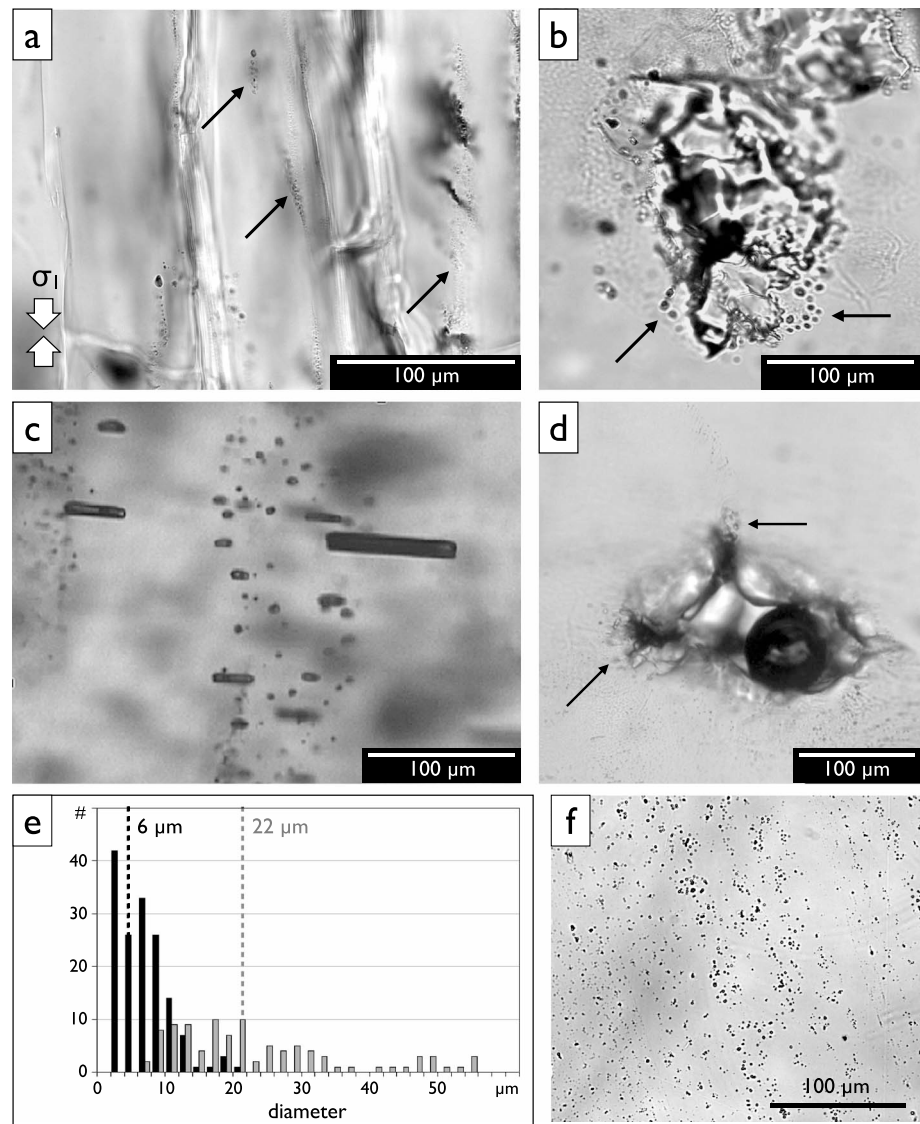
Figure 7. Fluid inclusions at experimental pressure and temperature before and after deformation and after annealing. Shortening direction applies to all images. (a) Undeformed sample (143 ATH) showing vertical cracks and small fluid inclusion trails (arrows) after pressurization and heating. (b) Decrepitated fluid inclusion with neonate inclusions (arrows) (sample 170 ATH, undeformed but after pressurization and heating). Decrepitation due to hydrostatic internal underpressure. (c) Fluid inclusions flattened normal to sample axis due to deviation from hydrostatic stress state, undeformed (see text, sample 171 ATH). (d) Decrepitated fluid inclusion after deformation, surrounded by small neonate inclusions found in microcracks (arrows). (e) Histogram of fluid inclusion size in pressurized material (undeformed, grey bars) and after deformation (black bars). Numbers indicate mean sizes. (f) Fluid inclusions after deformation and annealing.

misorientation bands (SWUE) [*Trepmann and Stöckhert*, 2013] (see above) with their boundaries subparallel to the trace of the $<c>$ axis are common (Figure 5b).

3.4. Fluid Inclusion Size, Shape, and Redistribution

In samples brought to P, T conditions and subsequently quenched without deformation, fluid inclusions have decrepitated during pressurizing and heating, producing a large number of microcracks (Figures 7a and 7b). The cracking is in part the result of a deviation of P and T from the original isochore of the fluid inclusions [e.g., *Tarantola et al.,* 2010; *Diamond et al.,* 2010]. Several fluid inclusions have experienced hydrostatic internal underpressure or overpressure, decrepitated, leaked water and have formed neonate fluid inclusions (Figures 7b and 7d).
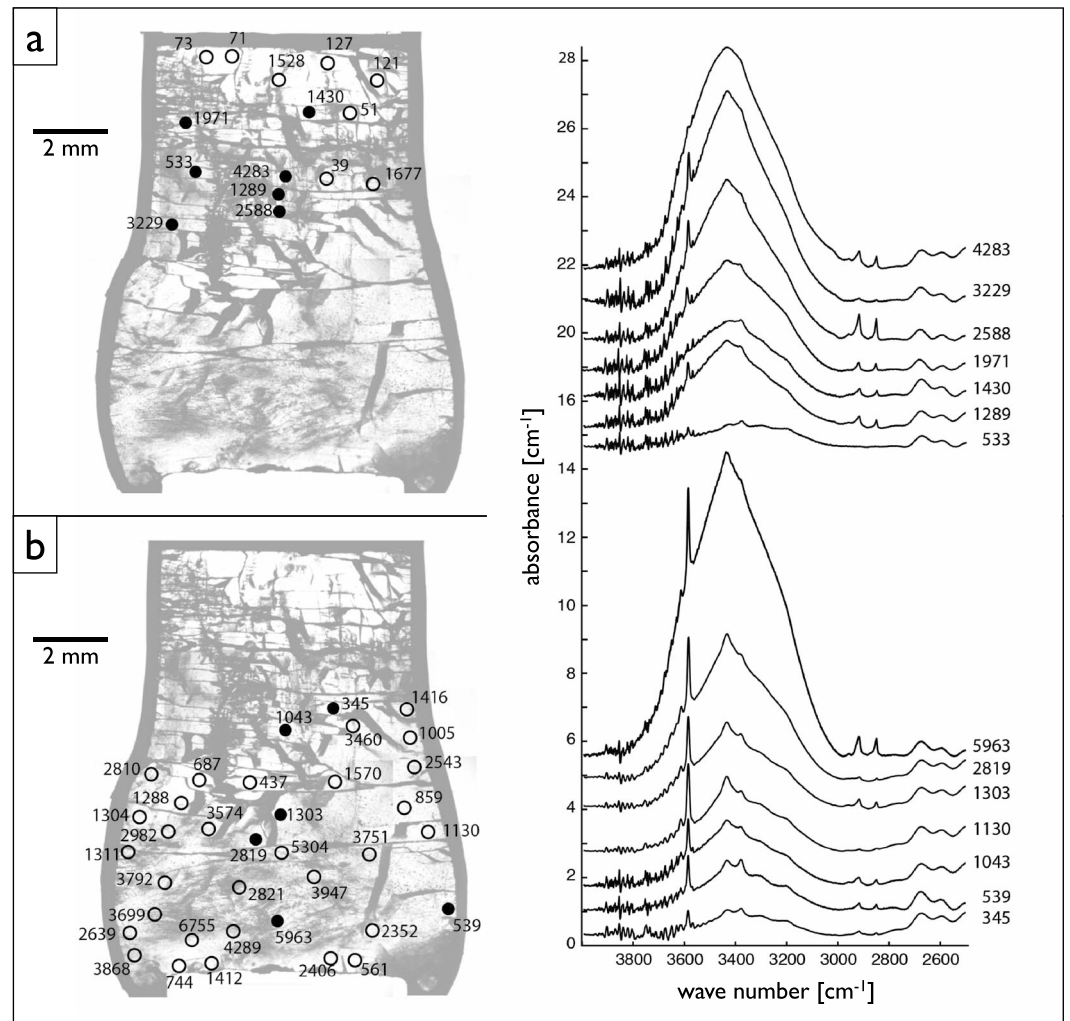
Figure 8. FTIR mapping of a sample deformed in ⊥m orientation (light beam parallel to the *c* axis, E normal to c). Unpolarized light was used for all measurements. Micrographs of thick section of the whole sample (190 ATH) showing the spatial distribution of fluid inclusions after deformation (gray regions) and sites of FTIR measurements; the numbers indicate the content of $H/10^6 Si$, and filled symbols denote selected spectra shown on right. Note the presence of a pointed broadband and the prominent 3585 cm^{-1} absorption band in deformed parts of the sample. (a) Sites and spectra for the ± undeformed part of sample. (b) Sites and spectra for the deformed part of sample.

In addition to a deviation from the isochore, fluid inclusions have also decrepitated because of nonhydrostatic conditions during pressure increase. The solid medium sample assembly usually does not facilitate a true hydrostatic stress state in the sample during pressurization, and a higher normal stress in the axial compression direction is common. As a consequence, many inclusions are flattened subperpendicular to the compression axis (Figure 7c) [cf. *Tarantola et al.,* 2010; *Hirth and Tullis,* 1994].

There are different kinds of microcracks. Some healed cracks contain trails of many small fluid inclusions arranged in planes parallel to the cylinder axis (Figure 7a). These cracks probably have formed during early stages of pumping under low confining pressure (Figure 7a) [cf. *Tarantola et al.,* 2010, 2012] and occur parallel to the compression axis (mode I cracks or axial splitting). Such microstructures are similar to those described as "microcrack ladder" features by *Fitz Gerald et al.* [1991], but, different from their observations, the trails of microcracks in our samples are regions with a high density of fluid inclusions.

From samples retrieved at different stages of pressurization and temperature increase, it is observed that there is a progressive development of fluid inclusion microstructures: During early stages of pressurization there still are some fluid inclusions that have sizes similar to those in the starting material. With
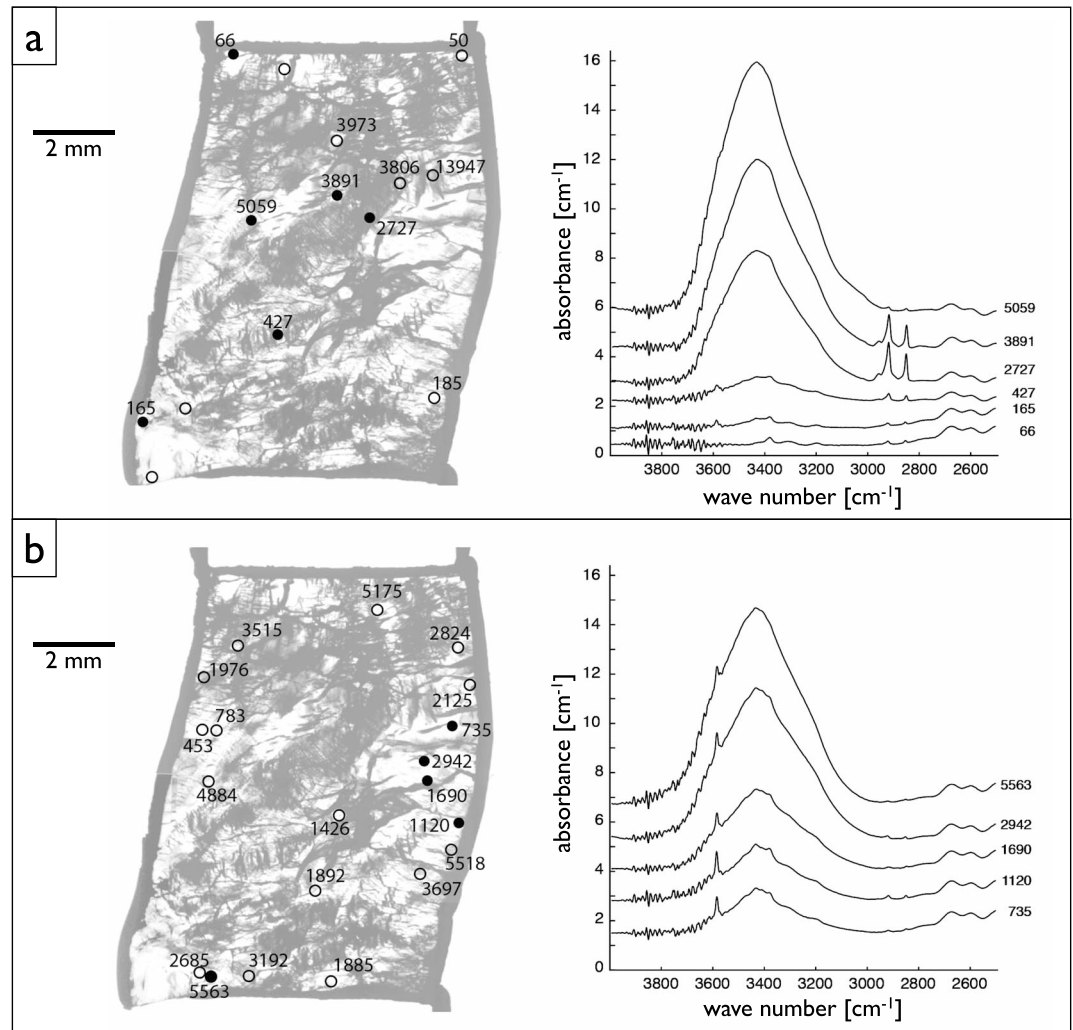
Figure 9. FTIR mapping of a sample deformed in O^+ orientation (light beam normal to the c axis, E parallel to c). Unpolarized light was used for all measurements. Micrographs of thick section of the whole sample (192 ATH) showing the spatial distribution of fluid inclusions after deformation (gray regions) and sites of FTIR measurements; the numbers indicate the content of $H/10^6Si$, filled symbols denote selected spectra shown on right. (a) Sites and spectra that do not show the $3585\,cm^{-1}$ peak. (b) Sites and spectra that show the $3585\,cm^{-1}$ peak.

increasing P, T conditions fluid inclusions tend to become smaller down to sizes of several tens of nanometer. Some fluid inclusions (up to ~50 μm in length) are elongated normal to the compression direction (Figure 7c).

After deformation the inclusions show a redistribution, reequilibration, and a further dramatic reduction in size (Figures 7d and 7e), down to the nm scale. At the light microscope scale, fluid inclusions decrease from a mean of 22 μm in the starting material to a mean of 6 μm (in the ⊥m samples; Figure 7e). The average size of inclusions in deformed samples is smaller in O^+ than in ⊥m samples (~4 μm versus 6 μm). In the most strongly deformed parts of the O^+ samples the inclusions are too small to be measured in the light microscope. An increase of salinity after deformation up to 14 wt % eq. NaCl (derived from ice melting temperature; see $T_{m(ice)}$ in *Tarantola et al.* [2012]) demonstrates a water leakage from precursor inclusions.

Annealed samples show different shapes and distributions of fluid inclusions compared to samples, which were quenched immediately after deformation. In ⊥m orientation these inclusions are aligned in trails subparallel to prism planes and are mostly spherical (Figure 7f).
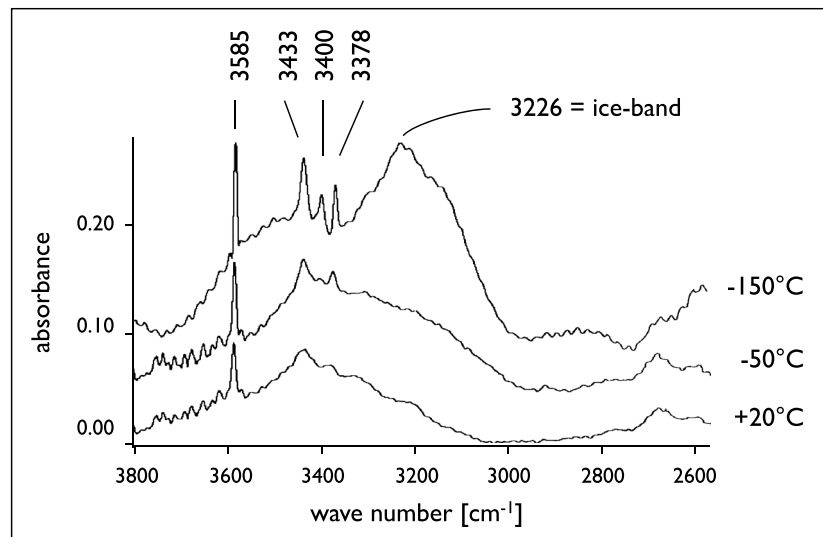
Figure 10. FTIR absorption spectra of deformed quartz in ⊥m orientation measured at different temperatures (light beam parallel to the c axis, E normal to c). Unpolarized light was used for all measurements. Spectra of sample 152 ATH are shown. Note: with decreasing temperature, the sharp absorption band at $3585 \, cm^{-1}$ shifts slightly to $3580 \, cm^{-1}$ ($-150°C$). Bands in the region between $3500 \, cm^{-1}$ and $3300 \, cm^{-1}$ become more discrete as a triplet at $3433 \, cm^{-1}$, $3400 \, cm^{-1}$, and $3378 \, cm^{-1}$, and the ice band at $\sim 3200 \, cm^{-1}$ appears.

3.5. FTIR Measurements and Water Analysis

The quartz starting material contains ~50 to $150 \, H/10^6 \, Si$, measured between visible fluid inclusions. In pressurized samples (not deformed) spectra show a rounded broad absorption band in the region between 3000 and $3800 \, cm^{-1}$ with a maximum absorption at $\sim 3400 \, cm^{-1}$ (Figures 8 and 9). These spectra indicate molecular water in inclusions, clusters, and aggregates, etc. [e.g., *Aines and Rossman*, 1984; *Kronenberg and Wolf*, 1990; *Nakashima et al.*, 1995]. In undeformed regions without fluid inclusions weak discrete bands at 3378, 3305, and $3195 \, cm^{-1}$ are visible (e.g., spectrum with 66 ppm H in Figure 9a). These bands originate from point defects in the quartz structure, probably OH groups coupled with Al substitution.

Deformed samples (130 MPa–230 MPa flow stress) show a characteristic modification in absorption spectra. The absorption band between $3800 \, cm^{-1}$ and $3000 \, cm^{-1}$ is present, but its maximum is more pointed than in only pressurized samples (Figures 8–10). This band is termed "pointed broad absorption band" here to distinguish it from the rounded broad absorption band in samples, which are only pressurized.

On top of the pointed broadband small discrete bands appear at $3433 \, cm^{-1}$ and $3378 \, cm^{-1}$ (Figures 8 and 10) in deformed regions of samples. Such spectra can be well observed in sample 190 ATH deformed in ⊥m orientation, where only the lower half of the sample is deformed (Figure 8). Undeformed parts of deformed samples show spectra with more rounded absorption bands, comparable to the starting material or to pressurized samples (Figure 8) so that there is a clear correlation between the character of absorption bands and local strain (the bulged region in ⊥m and the shear zones in O^+ samples show a pointed broadband, the undeformed regions rounded broadbands; Figures 8 and 9).

On a cooling stage at $-150°C$ (123 K), the molecular water in fluid inclusions freezes and in FTIR measurements ice bands appear (Figure 10) in the wave number region at 3200 to $3226 \, cm^{-1}$ [e.g., *Kronenberg and Wolf*, 1990; *Bergren et al.*, 1978; *Aines and Rossman*, 1984; *Prasad et al.*, 2006]. Such ice bands do not form in very small inclusions (nonfreezable water), containing only several hundreds of molecules of water trapped within the quartz [e.g., *Kronenberg and Wolf*, 1990].

A triplet of bands at 3433, 3400, and $3378 \, cm^{-1}$ becomes visible in the low-temperature spectra (Figure 10). The intensity of these bands increases, and the width of the bands decreases with decreasing temperature. At room temperature these bands tend to merge toward a single peak, which overlaps with the broad absorption band of molecular water. The distinct sharp bands around $3400 \, cm^{-1}$ are commonly assigned to OH defects in the
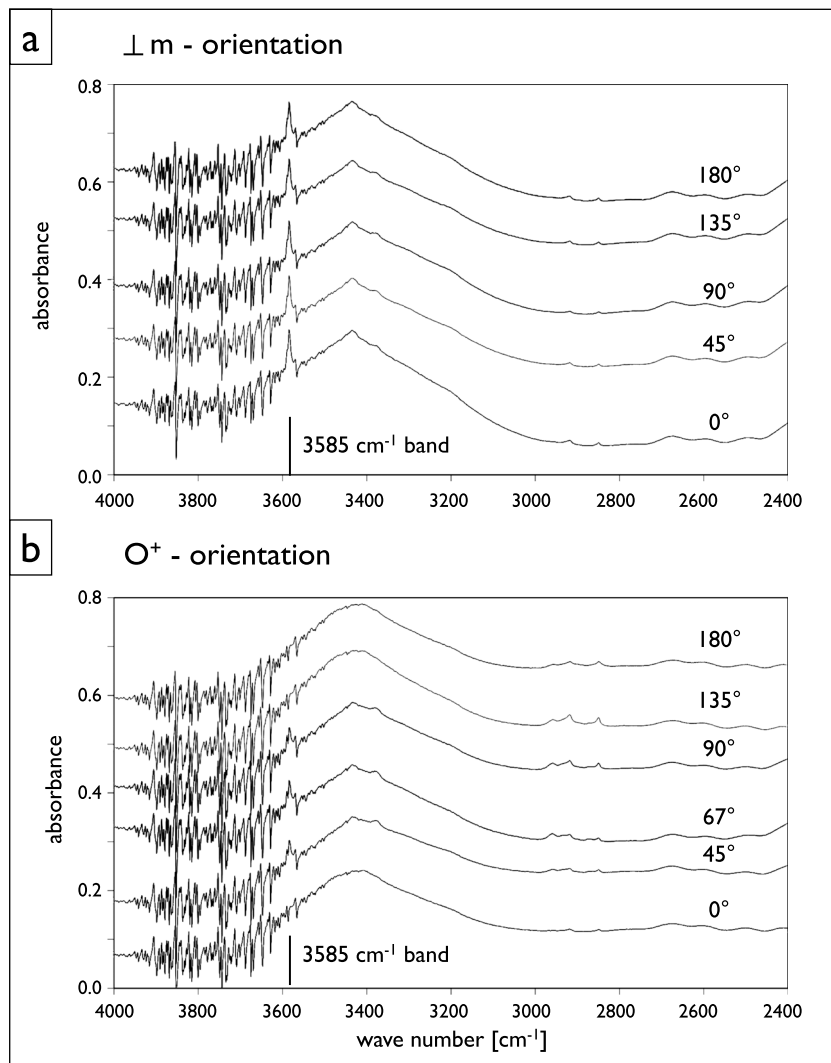
Figure 11. FTIR measurements using unpolarized light but a polarizer in the emerging beam. (a) Sample 190 ATH (⊥m) (light beam parallel to the *c* axis, E normal to c). There is no change in absorption of the 3585 cm^{-1} band for different rotation angles. (b) Sample 192 ATH (O^{+}) (light beam normal to the *c* axis, E parallel to c). There is no absorption of the 3585 cm^{-1} band when the *c* axis is normal to the polarizer (0 and 180°) and a maximum absorption between near 90° to the polarizer (basal plane parallel to the polarizer).

quartz structure, associated with aluminum (coupled substitution of Al^{3+} and H^{+} for Si^{4+} [*Kats et al.,* 1962; *Brunner et al.,* 1961; *Chakraborty and Lehmann,* 1976a, 1976b; *Pankrath,* 1991]).

In addition, a sharp absorption band at 3585 cm^{-1} (Figure 10) appears in deformed regions of crystals (Figures 8–10). The discrete band of 3585 cm^{-1} shifts slightly to 3580 cm^{-1} in measurements at 123 K and becomes more discrete and intense (Figure 10). The intensity of this band correlates with that of the triplet at 3433, 3400, and 3378 cm^{-1} and increases with increasing degree of local deformation (Figure 8).

Measurements with an unpolarized IR beam but a polarizer in the beam emerging from the sample show a pleochroism of the 3585 cm^{-1} absorption band in O^{+} sections but not in ⊥m sections (Figure 11). In the O^{+} orientation, the band is weaker than in the ⊥m orientation, and it is strongest when the polarizer is parallel to the basal plane (Figure 11b). The observation is consistent with structurally bound OH dipoles for this band (concluded above), and indicates an orientation of OH dipoles approximately normal to the *c* axis (in the basal plane).
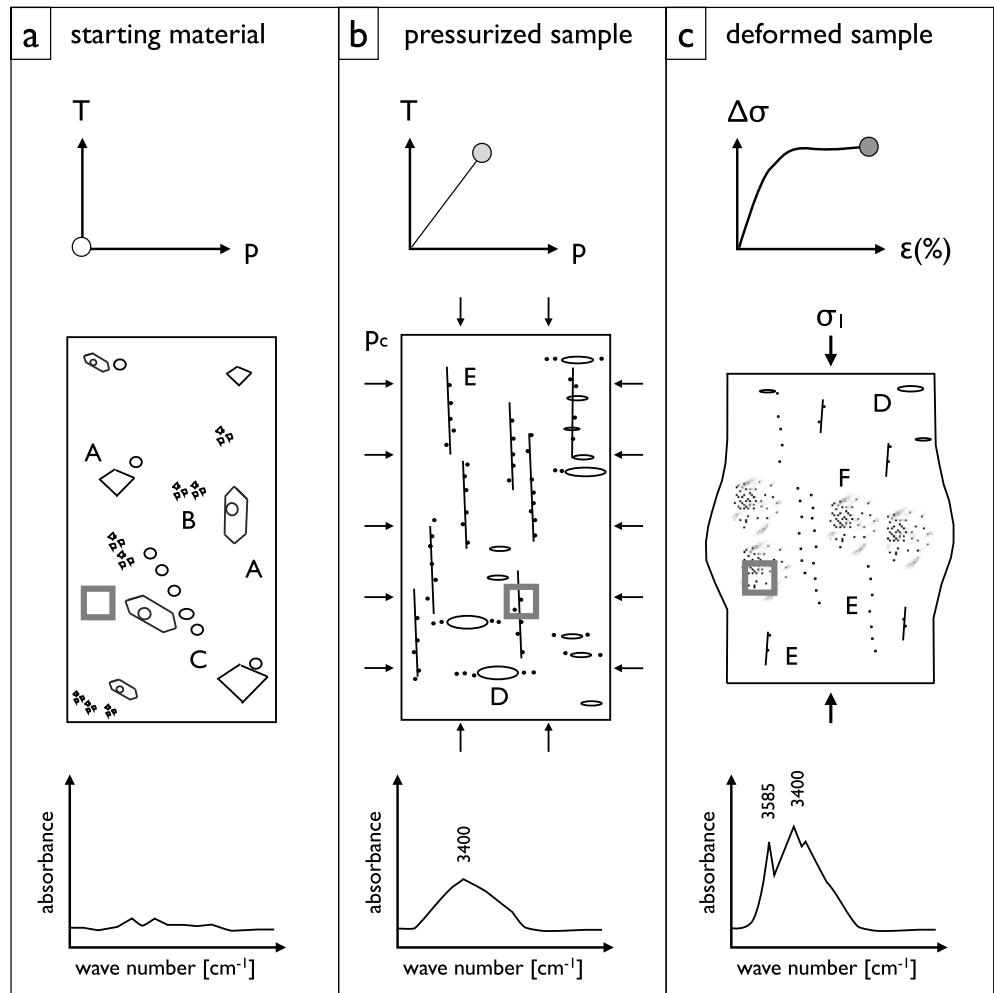
Figure 12. Schematic representation of fluid inclusion microstructures and FTIR spectra for starting material (a), pressurized (b), and deformed samples (c). Size and distribution of fluid inclusions (FI) are shown schematically at the same scale. Legend: A = negative crystal shape; B = clusters of FI; C = trails of FI; D = flattened FI (healed cracks, decrepitated FI with neonate FI); E = vertical trails of FI (healed cracks); and F = fine-scaled FI, often arranged in clusters. Small squares indicate typical measurement windows and their location for spectra below.

The systematic modification of fluid inclusions and FTIR spectra is schematically summarized in Figure 12. During pressurization, fluid inclusions are reduced in size and are associated with healed cracks. In deformed parts of samples the inclusions are further reduced in size, and a pointed broad absorption band appears, together with a discrete band at 3585 cm^{-1}.

3.6. Annealing of Samples

In annealed samples the sharp absorption band at 3585 cm^{-1} decreases substantially compared to the deformed and nonannealed samples (shown as average spectra of all measurements; Figure 13), or it may be completely absent in some spectra. The decrease is clearly observed in the ⊥m orientation, where the band is strongest in deformed and not annealed samples (Figure 13a). After annealing, the pointed broad absorption band at ~3400 cm^{-1} resembles a rounded broadband, as it is observed in undeformed samples (Figure 8a) documenting the connection between the 3585 cm^{-1} and ~3400 cm^{-1} bands, as described for the deformed samples above.

3.7. TEM Observations

The starting material has a very low dislocation density. Typical values of undeformed regions are in the range of 10^{10} m^{-2}. In deformed regions, the dislocation density increases by two to four orders of magnitude to
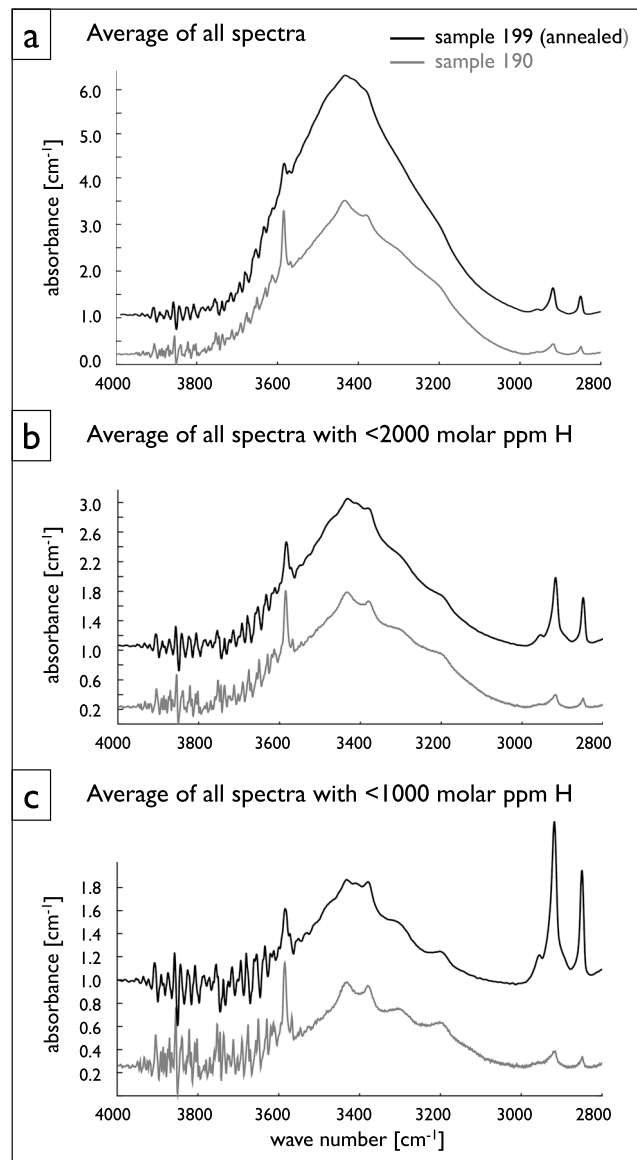
Figure 13. FTIR spectra of samples ⊥m using unpolarized light without and after annealing (light beam parallel to the c axis, E normal to c). Spectra of deformed sample 190 ATH without annealing (grey) and those of a sample 199 ATH in the same orientation after annealing (black). (a) Average of all spectra. (b) Spectra with low H_2O content (<2000 M ppm H). (c) Spectra with very low H_2O content (<1000 M ppm H).

$\sim 10^{12}$ to $10^{14}\,m^{-2}$, and in the deformation lamellae (see below) the dislocation densities may even exceed these values.

The deformation lamellae and misorientation bands appear as regions of high dislocation density in the TEM (Figures 14a and 14b). The lamellae are parallel to the basal plane or the prism planes. In the regions of lower dislocation density, where individual dislocations can be resolved, they appear to glide in the basal plane (Figure 14b). The dislocation densities change over a short distance across the margins of the lamellae without the formation of ordered subgrains or other systematic defect arrays (Figures 14a and 14b).

Dislocations commonly are associated with small fluid inclusions, which can be smaller than $0.1\,\mu m$ (Figure 14c). Some larger fluid inclusions are located directly in dislocation arrays (Figures 14c and 14d), and their close association suggests that the fluid inclusions and dislocations originate from former microcracks, which have subsequently healed. During the healing process the fluid inclusions are trapped, and dislocations may form as a consequence of the minor incongruence of the crystal structures across the crack (misfit dislocations) or by dragging during crack propagation. Larger fluid inclusions may show some evidence of crack formation associated with the pores (e.g., Figure 15). These pores are aligned along mode 1 cracks and are surrounded by a higher dislocation density (Figure 15b). The dislocation density decreases away from the healed crack and fluid inclusions trails (Figures 15b–15d).

In addition to the larger pores, there are some very small fluid inclusions or H_2O clusters (down to 10 nm), which are directly associated with single dislocations (Figure 14e). These inclusions may result from H_2O release from dislocations during partial recovery or annealing as observed by *McLaren et al.* [1983].

4. Discussion

4.1. Crystal Plastic Deformation

Bulk sample strain has been acquired by crystal plastic deformation, as shown by the following: (1) Absence of sample-scale fractures with noticeable offset, (2) the fact that sample shapes after deformation are consistent with the activation of defined slip systems, (3) flow stresses well below the confining pressures (Goetze criterion), and (4) the strong increase in dislocation density (at least locally). The fact that cracks do not
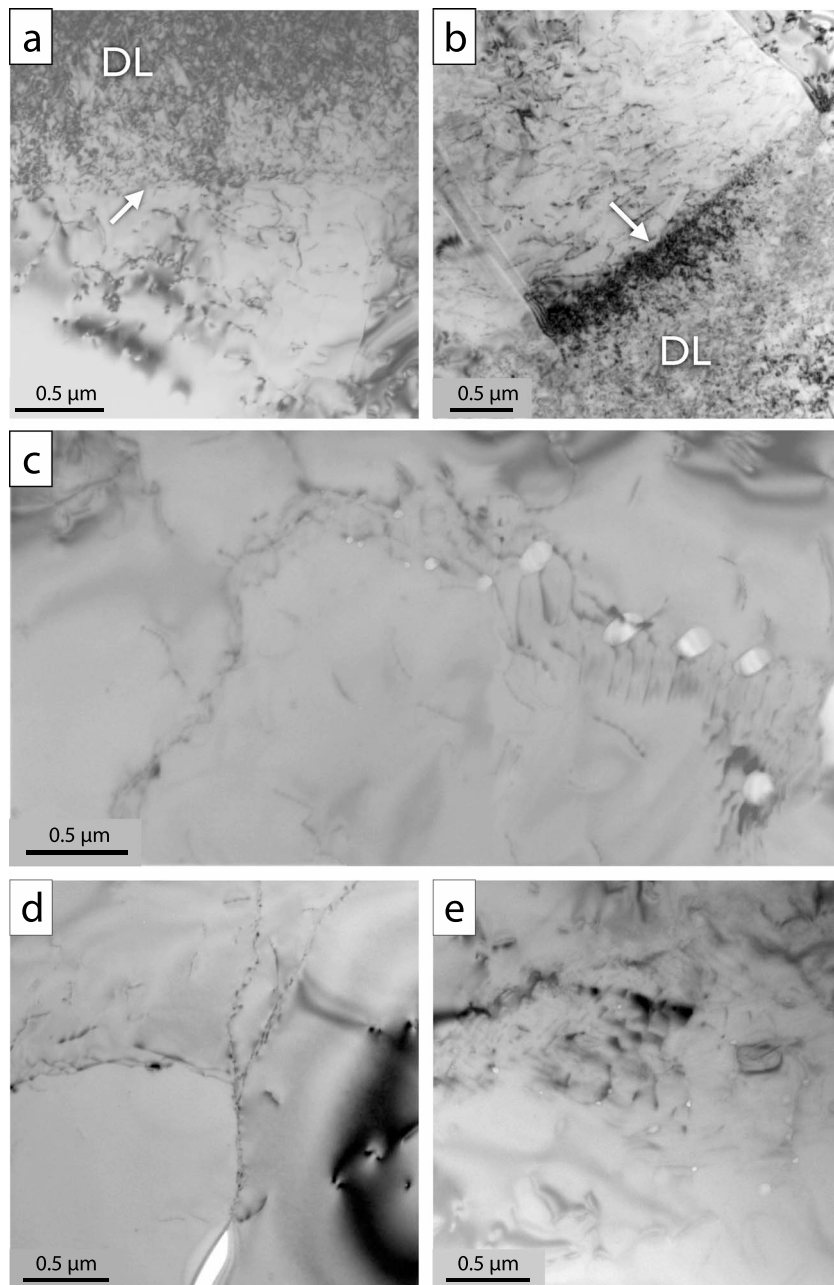
Figure 14. Details of deformation lamellae and pores with dislocations in deformed samples. (a, b) TEM bright field images of deformation lamellae (DL) characterized by high dislocation density, arrows point to discrete boundaries (sample 192 ATH, O$^+$ orientation): (a) with a more gradual change of dislocation density, (b) with abrupt change of dislocation density from ~10^{12} m^{-2} to values higher than 10^{14} m^{-2}. (c, d, e) Sample 146 ATH, $\perp$m orientation: (c) small fluid inclusions (>0.1 μm) and associated defect arrays formed during crack healing, (d) large elongated pore located within defect arrays indicates formation of the latter by crack healing, and (e) very small pores (few to 50 nm) can be directly associated with dislocations. It is unclear whether these pores originate from crack healing or represent H$_2$O released from dislocations during partial recovery.

contribute kinematically to the sample strain indicates that they either form during pressurization or they may form at sites of stress concentration during plastic deformation (important stress concentrations around fluid inclusions [e.g., *Goodier* [1933]; *Hirth and Tullis* [1994]]. Thus, cracking may accompany crystal plastic deformation of quartz without much kinematic contribution to strain and can occur at low strength of the sample.
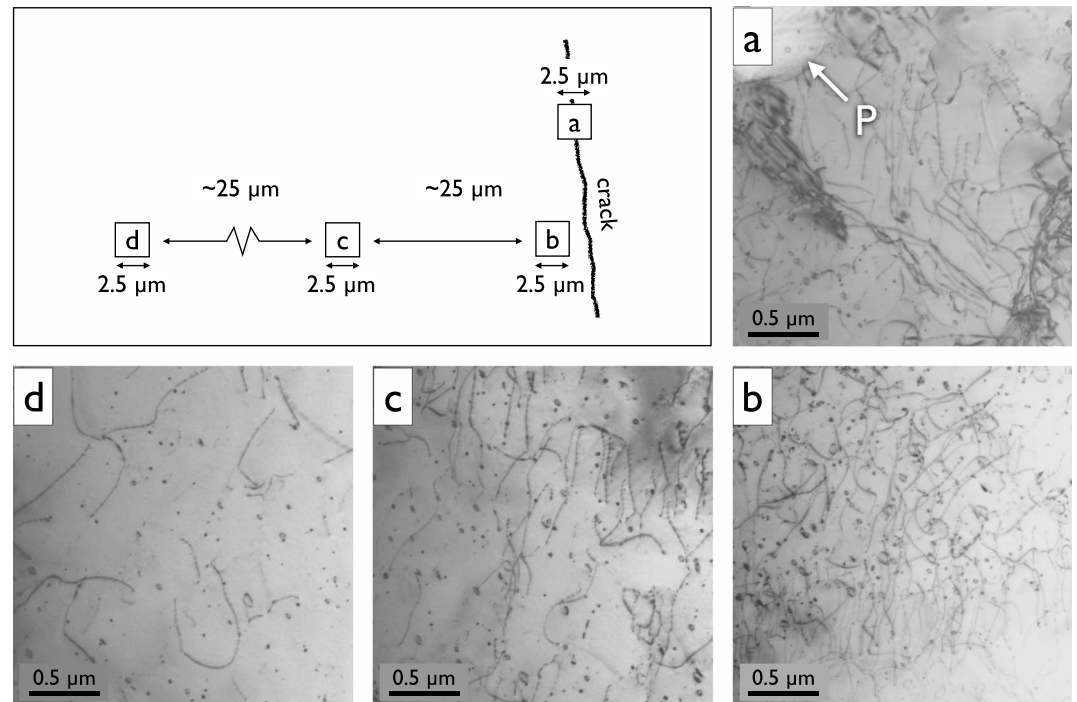
Figure 15. Dislocation densities in the vicinity of a healed crack. Schematic drawing shows relative location of images (sample 192 ATH, O^+ orientation). (a) Pore in healed crack (P) is associated with dislocations. (b–d) Dislocation density decreases systematically away from the healed crack over a distance of ~50 μm.

Little to no recrystallization is observed (especially in samples of lower strain), but there is a temperature dependence of deformation so that either the plastic strain attained by dominant dislocation glide is accompanied by some dynamic recovery or the glide process of dislocations in quartz is temperature dependent, as, e.g., by the formation of double kinks [*Paterson*, 2013, p. 122]. The latter seems to be an important aspect in materials with strong covalent bonding [*Paterson,* 2013]. Samples in $\perp m$ orientation deform by prism $<a>$ slip, whereas samples in O^+ orientation deform by basal $<a>$ slip without apparent activation of prism $<c>$ slip. This situation is different from synthetic samples, where some prism [*c*] slip is activated in O^+ orientations in addition to basal $<a>$ slip [e.g., *Blacic*, 1975; *Morrison-Smith et al.,* 1976; *Muto et al.,* 2011].

The fact that the small new grains with high angle boundaries occur almost exclusively in healed cracks suggests that these new grains have nucleated as small fragments which have grown after cracking. Similar observations have been made in experimentally deformed quartz by *den Brok and Spiers* [1991], *Vernooij et al.* [2006], *Trepmann et al.* [2007], and *Trepmann and Stöckhert* [2013]. Small defect-free fragments have been shown to grow in regions, which are highly damaged from cracking [*Stünitz et al.,* 2003]. It is to be expected that if fluid inclusions decrepitate during cracking, the resulting fluid-rich environment will promote grain growth.

A direct comparison of single crystal and polycrystalline mechanical data is difficult, but at a first glance our sample strengths (Figure 3) are similar to polycrystalline samples of Black Hills Quartzite at the same experimental conditions [*Hirth and Tullis*, 1992; *Heilbronner and Tullis,* 2002; *Stipp et al.,* 2006], although recrystallization is virtually absent in our single crystal samples. The fact that these natural samples are stronger than most synthetic single crystals in experiments [e.g., *Baëta and Ashbee*, 1970; *Kekulawala et al.,* 1981; *Linker and Kirby*, 1981; *Blacic and Christie*, 1984] may be attributed to two important differences between natural and synthetic crystals: (1) The H_2O distribution is more homogeneous in synthetic crystals. The variation of sample strength with microstructure and inhomogeneous fluid inclusion distribution (Figures 3 and 12) demonstrates the dependence of strength of natural crystals on fluid distribution. *Muto et al.* [2011], at similar deformation conditions as our experiments, find similar strengths at H_2O contents of 200 to 500 H/Si[6] (after deformation), which is a much narrower range but on average lower than our H_2O contents. (2) The H_2O

weakening in synthetic crystals is attributed to a specific mode of dislocation generation and multiplication [*McLaren et al.,* 1983, 1989].

The inverse pressure dependence of sample strength observed by *Heard and Carter* [1968], *Tullis et al.* [1979], *Mainprice and Paterson* [1984], *Kronenberg and Tullis* [1984], *Post et al.* [1996], and *Holyoke and Kronenberg* [2013] is not clearly observed in our samples (Figure 3), because the variation of strength for different individual samples of the same orientation and deformation conditions is greater than the strength variation of a given sample orientation at different pressures. The strength variation is attributed to a heterogeneous distribution of fluid inclusions and thus of local H_2O content in the quartz crystals. It demonstrates clearly that H_2O content, in addition to pressure and temperature conditions, has a strong effect on the strength of quartz. The strength dependence on H_2O content has been noted by other researchers [e.g., *Griggs and Blacic*, 1965; *Griggs*, 1967; *Doukhan and Trépied*, 1985; *Cordier and Doukhan*, 1989; *Paterson*, 1989; *Hirth and Tullis*, 1992; *Post et al.,* 1996; *Kronenberg et al.,* 2001; *Holyoke and Kronenberg*, 2013]. This strength dependence represents a disequilibrium effect, because the solubility of H in quartz is extremely low, and the H content, if measurable, constitutes an H oversaturated condition.

4.2. Fluid Inclusion Redistribution During Sample Pressurization

The original starting material is a milky quartz with a high density but heterogeneous distribution of fluid inclusions. The measured water contents of the quartz starting material between fluid inclusions are $< 100 \, H/10^6 Si$, so that this material can be considered as "dry" and thus mechanically strong. The H_2O of pressurized and deformed samples is present as molecular water in fluid inclusions documented by broad FTIR absorption bands (rounded and pointed [e.g., *Aines and Rossman*, 1984; *Aines et al.,* 1984; *Kronenberg and Wolf*, 1990]. It is difficult to measure H_2O contents in inclusion-free volumes of the pressurized samples, because these volumes typically are smaller than the FTIR measurement window as a consequence of the H_2O redistribution. Molecular water is redistributed from larger into much smaller fluid inclusions and into parts of the crystals, which previously were inclusion free (Figure 12).

The process of cracking, fluid wetting of the crack surface, subsequent crack healing, and formation of small neonate inclusions can be shown in all pressurized samples [*Tarantola et al.,* 2010, 2012; *Diamond et al.,* 2010]. Thus, during pressurization, H_2O is dispersed in the samples by cracking and crack healing to a more homogeneous distribution (Figures 7 and 12). During this process the FTIR absorption broadband does not change its shape and position much with respect to the starting material (Figures 12).

4.3. H_2O Redistribution and Dislocation Activity During Deformation

In all deformed samples the regions of very small dispersed fluid inclusions (light microscope scale) and submicroscopic fluid inclusions (TEM scale) coincide with regions of localized crystal plastic deformation (Figures 7, 8, 14, and 15), indicating an intense redistribution of fluid where samples are deformed. This is observed in narrow misorientation bands, which occur in conjunction with deformation lamellae and in the vicinity of fluid inclusion trails and arrays (Figures 5 and 6). They are bands of alternating high and low dislocation densities (Figures 14a and 14b), consistent with observations made by *Christie et al.* [1964] and *McLaren et al.* [1970] for deformation lamellae and by *Morrison-Smith et al.* [1976], *Fitz Gerald et al.* [1991], and *Trepmann and Stöckhert* [2013] for the misorientation bands or short wavelength undulatory extinction bands (SWUE).

The absence of ordered subgrain structures and tangled dislocations in our samples suggest that such defect structures are low-temperature plasticity features. *Trepmann and Stöckhert* [2013] have produced such structures at very high differential stresses and low temperatures in their experiments, whereas in our samples, these dislocation structures are produced during pressurization and at low differential stresses and higher temperatures [cf. *Tarantola et al.,* 2012], but in our case they are always connected to H_2O defects (Figures 5, 6, 14, and 15).

In the TEM, decrepitated fluid inclusions are associated with disordered dislocation arrays from crack healing (Figures 14c and 14d) [cf. *Fitz Gerald et al.,* 1991]. Some of the fluid inclusions associated with single dislocations (Figure 14e) may have formed during partial recovery, when fluid is released from dislocations [*McLaren et al.,* 1983, 1989; *Kronenberg et al.,* 1986; *McLaren*, 1991; *Drury*, 1991], but many pores in dislocation arrays are too large in size to result from recovery, and such dislocation arrays most likely result from crack healing. It is

difficult to decide whether the dislocations are induced by the cracking process itself by dragging dislocations at the crack tip or result from the misfit of the two crack surfaces during the healing process [*Darot et al.*, 1985; *Fitz Gerald et al.*, 1991]. The interaction of fluid inclusions with dislocations has also been observed by *Bakker and Jansen* [1990, 1991, 1994]. In any case, from the observations it can be concluded that dislocations are introduced by cracking and crack healing. The healing in the presence of an aqueous fluid is a fast process in quartz [*Smith and Evans*, 1984]. Some of the dislocations generated by cracking or crack healing are glissile after their formation, as indicated by the decreasing dislocation density further away from the healed cracks (Figure 15). The occurrence of such features in samples, which are only pressurized and are nominally undeformed, indicates that these processes can occur at low deviatoric stresses.

As described by *Fitz Gerald et al.* [1991], some cracking precedes dislocation glide, as also inferred from Figure 15. In our samples and in those of *Trepmann and Stöckhert* [2013], dynamic recovery at high temperatures modifies the initial microstructures during subsequent creep. The resulting creep microstructures are similar in our and *Trepmann and Stöckhert* [2013] samples (cf. their Figures 6 and 7), but in our samples, differential stresses have always been far below the Goetze criterion. Thus, local stress concentration at low bulk stresses of ~100 to ~400 MPa is sufficient to introduce cracking and/or high defect densities in quartz.

There is a correlation between $<c>$ axis misorientation and fluid inclusion arrays. The highest $<c>$ axis misorientation occurs between single fluid inclusion trails (healed cracks; Figures 5–7) and where fluid inclusion trails and small-scale fluid inclusions are concentrated. It is inferred that glissile dislocations, which are introduced by cracking and crack healing, slip and deform the regions adjacent to the cracks (Figures 15), producing misorientation and SWUE bands during dynamic recovery. Unloading cracks on both sides of the healed mode 1 cracks indicate a local lateral extent of plastic deformation of 50 to 100 μm (Figure 5a), consistent with TEM observations (Figure 15). These observations and interpretations are similar to those made by *Fitz Gerald et al.* [1991].

4.4. Broad and Discrete Absorption Bands and H_2O Speciation

The rounded and the pointed absorption band observed here are both referred to as "broad absorption band" in the literature without making a systematic distinction between them [*Aines and Rossman*, 1984; *Rovetta*, 1989; *Kronenberg*, 1994]. The type of broad absorption band which we have termed "rounded broadband" has been observed in different types of quartz and is assigned to molecular water in clusters or inclusions or grain boundaries [*Kekulawala et al.*, 1981; *Kronenberg and Wolf*, 1990; *Kronenberg*, 1994].

Rovetta et al. [1986] showed the appearance of an absorption band, which we termed "pointed broadband", in fractured quartz samples. The discrete bands at 3433 and 3378 cm^{-1} (at room temperature they are a part of the peak section of the pointed broad band) are assigned to OH stretching vibrations associated with Al^{3+} defects, and the band at 3400 cm^{-1} is so far unassigned to a specific charge compensation defect [*Kats et al.*, 1962; *Kronenberg*, 1994; *Subramaniam et al.*, 1984]. These bands are stronger and more discrete in low-temperature measurements at ~123 K (Figure 10). It is concluded that the pointed nature of the absorption band is caused by a combination of molecular water and structurally bound OH defects of the three discrete bands of 3433, 3400, and 3378 cm^{-1}.

Some of the structural OH bonding may occur at the surface of very small sized fluid inclusions, where H_2O is not a free fluid (and thus not freezable [*Aines and Rossman*, 1984; *Kronenberg and Wolf*, 1990; *Cordier and Doukhan*, 1991; *Kronenberg*, 1994]). However, the fact that the 3585 cm^{-1} absorption band is polarized and pleochroic cannot be explained by adsorption of H_2O to surfaces, because O-H bonds by adsorption of H_2O should not result in a crystallography controlled polarization of the absorption band. Therefore, more than 95% of the OH defects is bound within the quartz crystal structure as inferred from FTIR studies of these defects [*Wood*, 1960; *Kats et al.*, 1962; *Aines and Rossman*, 1984, 1985; *Rovetta et al.*, 1986; *Halliburton et al.*, 1981]. Both, the fact that the pointed broadband only occurs in deformed parts of samples and the lack of a source for Al exchange in our samples, indicate that the OH defects are related to dislocations. Thus, the change in shape of the absorption spectra from rounded to pointed bands occurs during deformation of the samples and indicates that the pointed broadband is the result of incorporation of additional OH defects into the quartz crystal structure by dislocations.
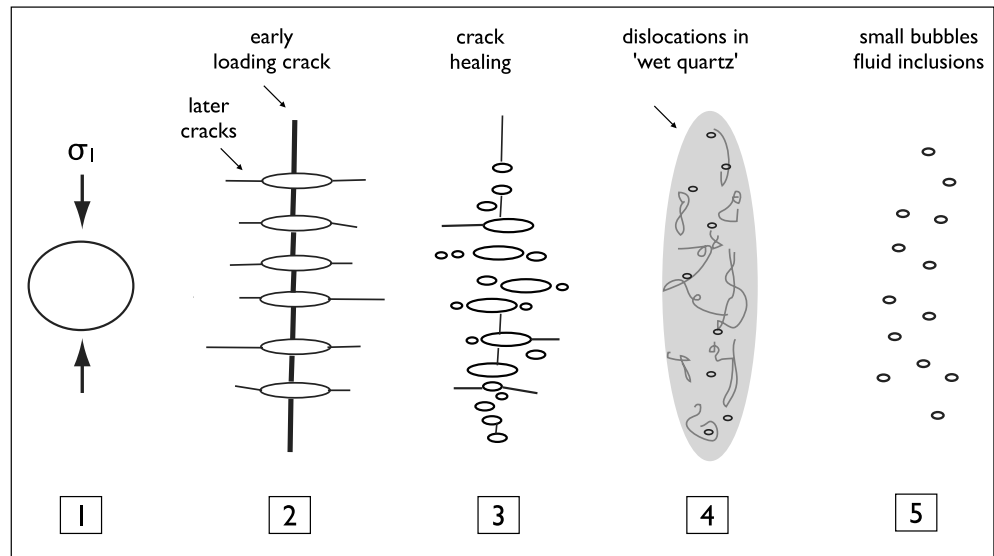
Figure 16. Recycling of aqueous fluid during deformation. Schematic of process: (1) fluid inclusions in starting material; (2) formation of cracks, decrepitation of fluid inclusions during pressurization and heating; (3) fast crack healing under experimental pressure and temperature before deformation; (4) multiplication of dislocations and formation of structurally bound OH during deformation; further size reduction of fluid inclusions; and (5) annealing: reduction of dislocation density and structurally bound OH, growth of fluid inclusions with H_2O.

4.4.1. The 3585 cm^{-1} Absorption Band

Of special interest is the discrete band at 3585 cm^{-1} which is prominent in room temperature and ~123 K measurements. It should be noted that the 3595 cm^{-1} band discussed by *Niimi et al.* [1999] and *Gleason and De Sisto* [2008] is a different absorption band than the 3585 cm^{-1} band referred to here [e.g., *Karampelas et al.,* 2005].

From earlier observations in the literature (in the appendix), it emerges that the 3585 cm^{-1} absorption band is caused by structurally bound OH, which occurs in dislocations on twin planes of amethyst, citrine, and chalcedony or, probably, as clusters in synthetic crystals [*McLaren et al.,* 1983, 1989], if no significant amounts of H bridges occur to cause broadband absorption. The defect-related nature of the 3585 cm^{-1} band in all of these occurrences and the fact that it is mainly present in deformed parts of the samples of this study (Figure 8) suggests that the 3585 cm^{-1} band records OH inside dislocations (as suspected by M. Paterson (personal communication, 2010)), together with the triplet of 3433, 3400, and 3378 cm^{-1} bands. It is conceivable that some of these defects may be left behind in the crystal structure after the dislocations have slipped through those regions. The polarization of the IR absorption appears to be only dependent on the Burgers vector $<a>$ rather than the slip planes (prism and basal planes), because the polarization is normal to [c], regardless of the slip planes.

During high-temperature annealing, the OH defects are released as H_2O, which produces fluid inclusions [*McLaren and Phakey*, 1965, 1966b], observable as an ice band in low-temperature measurements [*Kekulawala et al.,* 1981; this study, Figure 14], and a reduction or vanishing of the 3585 cm^{-1} band (e.g., Figure 16). Thus, the 3585 cm^{-1} band in deformed samples is a measurable expression of OH in dislocations or regions that have been affected by dislocation glide.

Using the *Libowitzky and Rossman* [1997] calculation, the discrete 3585 cm^{-1} absorption band represents between 1 and 3% of the total H content in our samples. If all Si-O bonds in quartz in dislocation cores form Si-OH bonds at a high dislocation density of $10^{14} m^{-2}$, the resulting H content would be ~5 H/10^6Si (this value is similar to those given by *Griggs* [1967], *Doukhan* [1995], and *Paterson* [1989]). Even in amethyst, where the H content of the 3585 cm^{-1} band is very high because of the numerous twin boundaries, the fraction of OH is only 4% of the total H content [*Chakraborty and Lehmann,* 1976a, 1978]. In natural clear quartz, it is at least an order of magnitude lower. Thus, the value of 1–3% of total H in our samples may

correspond to the order of magnitude of the typical fraction of the structurally bound OH of the 3585 cm^{-1} band contained in dislocations (of ~5 H/10^{6}Si) at total H contents of a few hundred H/10^{6}Si in wet quartz crystals.

The amount of hydrogen related to the defect peaks 3433, 3400 and 3378 cm^{-1} is difficult to quantify. These peaks cannot be properly separated by peak fitting because spectral features give insufficient constraints on the number of peaks in the spectral range 3500–3200 cm^{-1}. At least six bands from the originally present point defects and from the deformation-induced point defects are superimposed on the fluid-inclusion-related band system. The complex nature of this band system is the main reason why a more detailed analysis and quantitative characterization of the pointed broadband is impossible at his stage.

As the weakening effect of the very small clusters of H$_2$O in synthetic quartz works by dislocation generation and multiplication [*McLaren et al.*, 1983, 1989], it is proposed that this mechanism works in a similar way for very small fluid inclusions generated by decrepitation of larger fluid inclusions in our samples. The same mechanism has been demonstrated for crack healing in single crystals by *Fitz Gerald et al.* [1991]. It seems critical that the neonate inclusions are very small for the dislocation generation and multiplication. This interpretation is consistent with results by *Kronenberg et al.* [1986]: After heating a dry natural quartz crystal in talc for 11 h, the material is weak (from infiltration of H$_2$O through cracks), as found by *Griggs and Blacic* [1965], but after heating it for 112 h, the material is substantially stronger (because the fluid inclusions have grown in size). This behavior is well known for synthetic quartz, where fluid inclusion growth after annealing hardens the material and produces freezable water [*Kekulawala et al.,* 1981]. Thus, during heating in talc, very small fluid inclusions and defects will be formed from microcracking (inducing H$_2$O weakening in such crystals), but if these inclusions grow, their weakening effect by dislocation generation decreases.

One interesting effect of the proposed process is that the 3585 cm^{-1} absorption band can be induced in natural quartz by pressurization at high temperatures in talc [*Kekulawala et al.*, 1981; *Kronenberg et al.,* 1986] where very small fluid inclusions can form in the crystals (most likely by microcracking). This kind of treatment was carried out in a talc confining medium using unjacketed samples and presumably fast pressurization. The resulting fluid inclusions are all well below 100 nm in diameter [*Kekulawala et al.*, 1981], similar to our samples after deformation (Figure 14). The fact that the process is connected with H$_2$O diffusion is ruled out by the experiments of *Kronenberg et al.* [1986] and *Gerretsen et al.* [1989], who have demonstrated the impossibility to diffuse H$_2$O into quartz at laboratory time scales.

The correlation between the deformation and the occurrence of the pointed broadband (the 3433, 3400, and 3378 cm^{-1} triplet) and the 3585 cm^{-1} band indicates that OH is redistributed changing the OH speciation during crystal plastic deformation. The 3585 cm^{-1} band probably represents hydrogen complexes at dislocations. Once dislocations are generated at fluid inclusions, they may carry structurally bound OH. Whether this OH causes weakening by reducing the Peierls stress is not clear from our experiments. The OH can be released from the dislocations by annealing.

Thus, the fact that the OH in the dislocations is structurally bound as Si-O-H bonds is consistent with the hydrolytic weakening theory [*Griggs*, 1967, 1974]. However, dislocation generation, multiplication at H$_2$O fluid inclusions and subsequent dislocation glide are demonstrated in this study (Figure 14), consistent with the H$_2$O-weakening mechanism described in *McLaren et al.* [1989] and *Fitz Gerald et al.* [1991]. Our experiments do not provide evidence to either prove that glide-dependent hydrolytic weakening mechanism has operated nor can we conclude a dominance of either of the two weakening mechanisms.

4.5. Importance of Inferred H$_2$O Weakening Processes for Natural Quartz Deformation

One important process for inducing crystal plasticity in our experimentally deformed natural quartz crystals is microcracking, associated with fluid inclusion decrepitation and water leakage [see also *Kronenberg et al*., 1986; *Bakker and Jansen.,* 1990, 1991, 1994; *Fitz Gerald et al.,* 1991]. As demonstrated in our experiments, this type of cracking does not contribute kinematically to the deformation and thus does not constitute a frictional deformation mechanism. Cracking of the grains may take place at, e.g., local stress concentrations at low bulk differential stresses during crystal plastic deformation as demonstrated by the flow stresses as low as ~150 MPa at 1.0 or 1.5 GPa confining pressure (Figure 3). Thus, it is likely that the processes

inferred from single-crystal experiments of this study can be directly applied to natural samples and may be indicative of similar processes in nature, e.g., water infiltration may be facilitated through cracking [*Kronenberg et al.,* 1986, 1990].

The 3585 cm^{-1} absorption band occurs in other naturally deformed quartz samples [*Kronenberg and Wolf*, 1990; *Kronenberg et al.,* 1990; *Kronenberg*, 1994; *Ito and Nakashima*, 2002]. Therefore, the transfer of molecular H_2O into structurally bound OH defects in dislocations can be inferred to take place in nature as in the experiments.

The close relationship between cracking and crystal plastic deformation through dislocation generation in quartz constitutes a different H_2O weakening mechanism compared to olivine, where H_2O weakening is interpreted to be primarily induced by promoting climb and recovery [e.g., *Mei and Kohlstedt*, 2000b]. The weakening processes observed in our quartz samples may apply also to olivine in addition to the point defect mechanisms, if an excess fluid is present, e.g., as fluid inclusions [e.g., *Wanamaker et al.*, 1990]. Therefore, the observed H_2O weakening processes may apply to other silicates, too, so that the generation and multiplication of dislocations at healed cracks and very small fluid inclusions may constitute a general weakening process for silicates, if they can host small inclusions with an aqueous fluid.

The excess fluid may have a positive H_2O effect on recovery and recrystallization of polycrystalline quartz, as it has been found by *Tullis and Yund* [1989]. However, it is beyond the scope of this study to comment on these aspects, and we restrict this discussion to our observations of H_2O weakening during dislocation glide with limited dynamic recovery.

The H_2O weakening effect in quartz increases with increasing amounts of H_2O, as demonstrated by the inhomogeneous distribution of H_2O in some samples and results in a greater strength of H_2O-deficient regions. The correlation of strength with H_2O content has also been found by, e.g., *Griggs and Blacic* [1965] and *Holyoke and Kronenberg* [2013]. The incorporation of a fugacity term in the quartz flow law [*Kohlstedt et al.,* 1995] has improved the applicability and consistency of quartz flow laws [*Hirth et al.*, 2001; *Holyoke and Kronenberg*, 2013; *Kidder et al.,* 2016]. However, in addition to the fugacity term, it appears appropriate and necessary to complement the quartz flow law by a calibration for different H_2O contents. The measurable H_2O contents in quartz constitute excess H_2O and therefore a disequilibrium situation, because the equilibrium solubility of H_2O in quartz is extremely low and typically below the detection limit of most measuring methods.

5. Conclusions

The experimental deformation of natural milky quartz crystals at 900 and 1000°C results in the activation of dominant prism and basal $<a>$ slip in different crystal orientations. Locally, high dislocation densities develop into deformation lamellae (Figures 5, 6, and 14), as observed by *Christie et al.* [1964], *McLaren et al.* [1970], *Morrison-Smith et al.* [1976], and systematic misorientation features (short wavelength undulatory extinction bands; SWUE [*Trepmann and Stöckhert,* 2013]). Dislocation glide accompanied by minor dynamic recovery is the dominant deformation process in the single crystals.

The sample deformation is anisotropic because of different slip system orientations, and it is inhomogeneous because of a temperature gradient, and, especially, the inhomogeneous H_2O distribution (fluid inclusions) of the crystals. For this reason, it is not possible to detect the expected systematic relationship of decreasing flow stress with increasing confining pressure. The observed strengths of the two sample orientations ⊥m and O$^+$ and thus activated slip systems are not systematically different and are in a similar range as those of wet polycrystalline samples ($\Delta\sigma$ far below the confining pressure). Cracking takes place during pressurization and during sample deformation (Figures 5, 7, and 16), but there rarely is visible displacement at cracks. This observation and the low differential stresses of deformation indicate that the deformation has been fully plastic without contribution of frictional processes.

Many fluid inclusions decrepitate during pressurization as described in *Tarantola et al.* [2010, 2012]. The cracks heal and a large number of neonate fluid inclusions form. By these processes the number of fluid inclusions is strongly increased and the H_2O becomes more homogeneously distributed in the samples. During subsequent deformation, the size of fluid inclusions is further reduced (down to ~10 nm).

Dislocations are generated by crack healing, or they nucleate at small fluid inclusions. H_2O is further distributed through dislocations and their movement (Figures 14–16).

The rounded broad absorption band in the ~3400 cm^{-1} range in FTIR spectra is due to the presence of molecular water in larger fluid inclusions. A pointed broad absorption band (consisting in part of a triplet of discrete absorption bands at 3433, 3400, and 3378 cm^{-1}) is superposed on the rounded broadband in deformed regions of the quartz crystals (Figure 12) together with another discrete absorption band at 3585 cm^{-1}. There is a direct correlation of the discrete absorption bands and crystal plastic deformation (high dislocation densities), and it is inferred that the discrete bands are caused by structurally bound Si-O-H defects in dislocations. After annealing, the discrete bands are reduced or vanish due to H_2O released from the dislocations, forming very small fluid inclusions.

After the redistribution of H_2O by cracking, decrepitated fluid inclusions, and crystal plastic deformation, the FTIR spectra of our deformed natural single crystals are similar to those of synthetic quartz [e.g., *Kekulawala et al.,* 1981]. This effect is produced by the large number of very small nonfreezable fluid inclusions (like H_2O clusters) and locally high dislocation densities with structurally bound OH in dislocations (Figure 12).

The weakening effect of H_2O in these samples is best explained by the same mechanisms as in synthetic crystals, i.e., by dislocation generation and multiplication at very small fluid inclusions [*McLaren et al.,* 1989], although hydrolytic weakening [*Griggs*, 1974] is consistent with the observation of structural Si-O-H groups.

The inferred sequence of processes in the deformation of the single crystals is (Figure 16): (1) (Micro)cracking and fluid inclusion decrepitation, (2) crack healing and dislocation generation, (3) incorporation of OH in dislocations, (4) dominant dislocation glide, and (5) formation of fluid inclusions from dislocations during limited dynamic recovery. The generation and multiplication of dislocations continues to take place at fluid inclusions and H_2O-related defects. In this way, the H_2O is recycled between fluid inclusions as "reservoirs" (acting in part as dislocation sources) and the cores of dislocations during dislocation glide.

The cracking and crack healing play a major role in the process of dislocation generation. As some cracking proceeds during dominantly dislocation-accommodated deformation, there is a close interrelationship between brittle and crystal plastic deformation processes in quartz. Cracking may lead to fluid infiltration and thus to weakening of previously dry quartz [*Kronenberg and Wolf*, 1990; *Kronenberg et al.,* 1990]. Thus, it is inferred that the processes observed in these single crystals are likely to occur in a similar way in nature and may produce H_2O weakening.

Two major points, which are relevant to geodynamics and rheology, emerge from these experiments:

1. The identified H_2O weakening mechanism in quartz is very different from that in olivine and not directly related to recovery (H_2O effects on recovery have been observed as well [*Tullis and Yund*, 1989]). The disequilibrium nature of the process suggests that it is likely to occur in other silicates, too. Thus, it may operate in addition to the point defect mechanisms in, e.g., olivine, so that equilibrium concentrations of OH in the form of point defects indicate the maximum strength of wet material—it may be weaker if dislocation generation and multiplication mechanisms play an additional role.
2. The disequilibrium nature of the H_2O weakening mechanism in quartz (excess H_2O) may require an additional term specifying the H_2O content in the constitutive relationship for quartz.

Appendix A: Review of Observations of the 3585 cm^{-1} IR Absorption Band

The 3585 cm^{-1} absorption band has been observed in the past in quartz, but its importance for deformation had probably not been fully appreciated. It appears appropriate to review some of the earlier literature on this absorption band, but it goes beyond the scope of the text of a regular discussion on the deformation of wet quartz. That is why it is included as an appendix here.

The 3585 cm^{-1} absorption band is found in synthetic quartz crystals [*Wood*, 1960; *Kats et al.,* 1962; *Dodd and Fraser*, 1965; *Kopp and Staats*, 1970; *Chakraborty and Lehmann*, 1976a, 1976b; *Halliburton et al.,* 1981; *Kekulawala et al.,* 1981; *Subramaniam et al.,* 1984; *Aines and Rossman*, 1984; *Cordier and Doukhan*, 1989, 1991; *Pankrath*, 1991; *Bachheimer*, 1998; *Muto et al.,* 2011]. It is prominent in amethyst and citrine [*Chakraborty and Lehmann*, 1976a, 1976b; *Chakraborty and Lehmann*, 1978; *Aines and Rossman*, 1984; *Rovetta*, 1989; *Karampelas et al.,* 2005] and in chalcedony and microcrystalline quartz [*Frondel*, 1982;

Graetsch et al., 1985; *Chakraborty and Lehmann*, 1976a, 1976b, 1978; *Yamagishi et al.,* 1997; *Ito and Nakashima*, 2002], whereas it is weak or absent in clear natural quartz crystals [*Wood*, 1960; *Dodd and Fraser*, 1965; *Chakraborty and Lehmann,* 1976a, 1976b; *Bachheimer*, 1998]. This band has been assigned to hydrogrossular (4H)Si defects in the quartz structure [*Stalder and Konzett*, 2012], although the evidence for that has not been presented.

The polarization of the 3585 cm^{-1} band with the strongest absorption parallel to the basal plane has been described by *Chakraborty and Lehmann* [1976a, 1976b] and *Pankrath* [1991], demonstrating the structurally bound OH defects without many neighboring H bridges [*Kats et al.,* 1962; *Chakraborty and Lehmann*, 1976a, 1976b, 1978; *Halliburton et al.,* 1981; *Frondel*, 1982; *Kronenberg*, 1994]. The polarization is the reason why it is unlikely that the 3585 cm^{-1} is caused by (4H)Si defects in quartz. The absorption is directly correlated with the total H content in the crystals [*Chakraborty and Lehmann*, 1978] and is not related to monovalent metal ions such as Na$^+$ or Li$^+$ [*Dodd and Fraser*, 1965].

The prominent 3585 cm^{-1} band in chalcedony and amethyst is structurally related to the Brazil twinning, which is very common in these SiO$_2$ phases [*Frondel*, 1982; *Miehe et al.,* 1984; *Graetsch et al.,* 1987]. Defects associated with the twin planes have been observed by *McLaren and Phakey* [1965, 1966a] and by *McLaren and Pitkethly* [1982] and are associated with dislocations and OH, which is released as H$_2$O in very small fluid inclusions during electron beam damage or by heating crystals above ~600°C [*McLaren and Phakey*, 1965, 1966b].

The 3585 cm^{-1} absorption band in synthetic quartz is clearly weaker after annealing at atmospheric pressures [*Kekulawala et al.,* 1981, Figure 4, *Kronenberg*, 1994; *Bachheimer*, 1998], whereas it remains constant or may become stronger after annealing at pressure [*Kekulawala et al.,* 1981; *Cordier and Doukhan*, 1989, 1991]. In natural clear crystals, in which the 3585 cm^{-1} band is absent, it may appear after heating and pressurization in talc at 1.5 GPa [*Kekulawala et al.,* 1981, Figure 7]. *Rovetta et al.* [1986] observed a band at 3580 cm^{-1} in annealed samples and attributed the band to microcracking (disputed by *Cordier and Doukhan* [1991]).

References

Aines, R. D., and G. R. Rossman (1984), Water in minerals? A peak in the infrared, *J. Geophys. Res.*, *89*, 4059–4071, doi:10.1029/JB089iB06p04059.

Aines, R. D., and G. R. Rossman (1985), The high temperature behavior of trace hydrous components in silicate minerals, *Am. Mineral.*, *70*(11-12), 1169–1179.

Aines, R. D., S. H. Kirby, and G. R. Rossman (1984), Hydrogen speciation in synthetic quartz, *Phys. Chem. Miner.*, *11*(5), 204–212, doi:10.1007/BF00308135.

Bachheimer, J. P. (1998), An investigation into hydrogen stability in synthetic, natural, and air-swept synthetic quartz in air temperatures up to 1100°C, *J. Phys. Chem. Solids*, *59*(5), 831–840.

Baëta, R. D., and K. H. G. Ashbee (1970), Mechanical deformation of quartz: l. Constant strain-rate compression experiments, *Philos. Mag.*, *22*(177), 601–623.

Bakker, R. J., and J. B. H. Jansen (1990), Preferential water leakage from fluid inclusions by means of mobile dislocations, *Nature*, *345*(6270), 58–60.

Bakker, R. J., and J. B. H. Jansen (1991), Experimental post-entrapment water loss from synthetic CO$_2$-H$_2$O inclusions in natural quartz, *Geochim. Cosmochim. Acta*, *55*(8), 2215–2230.

Bakker, R. J., and J. B. H. Jansen (1994), A mechanism for preferential H$_2$O leakage from fluid inclusions in quartz, based on TEM observations, *Contrib. Mineral. Petrol.*, *116*(1-2), 7–20.

Bergren, M. S., D. Schuh, M. G. Sceats, and S. A. Rice (1978), The OH stretching region infrared spectra of low density amorphous solid water and polycrystalline ice, Ih, *J. Chem. Phys.*, *69*(8), 3477–3482.

Blacic, J. D. (1975), Plastic-deformation mechanisms in quartz: The effect of water, *Tectonophysics*, *27*(3), 271–294.

Blacic, J. D., and J. M. Christie (1984), Plasticity and hydrolytic weakening of quartz single crystals, *J. Geophys. Res.*, *89*, 4223–4239, doi:10.1029/JB089iB06p04223.

Bodnar, R. J. (2003), Introduction to aqueous-electrolyte fluid inclusions, *Fluid Inclusions Anal. Interpret.*, *32*, 81–100.

Brunner, G. O., H. Wondratschek, and F. Laves (1961), Infrared studies on the incorporation of H in natural quartz, *Z. Elektrochem. Angew. Phys. Chem.*, *65*, 735–50.

Byerlee, J. D. (1968), Brittle-ductile transition in rocks, *J. Geophys. Res.*, *73*, 4741–4750, doi:10.1029/JB073i014p04741.

Chakraborty, D., and G. Lehmann (1976a), Distribution of OH in synthetic and natural quartz crystals, *J. Solid State Chem.*, *17*(3), 305–311.

Chakraborty, D., and G. Lehmann (1976b), On the structures and orientations of hydrogen defects in natural and synthetic quartz crystals, *Phys. Status Solid. (a)*, *34*(2), 467–474.

Chakraborty, D., and G. Lehmann (1978), On the fine structure in the infrared spectra of clear natural quartz, amethyst, citrine and synthetic quartz crystals in the 3400 cm^{-1} region, *Z. Naturforschung A*, *33*(3), 290–293.

Chernak, L. J., G. Hirth, J. Selverstone, and J. Tullis (2009), Effect of aqueous and carbonic fluids on the dislocation creep strength of quartz, *J. Geophys. Res.*, *114*, B04201, doi:10.1029/2008JB005884.

Christie, J. M., and A. J. Ardell (1974), Substructures of deformation lamellae in quartz, *Geology*, *2*(8), 405–408.

Christie, J. M., D. T. Griggs, and N. L. Carter (1964), Experimental evidence of basal slip in quartz, *J. Geol.*, *72*(6), 734–756.

Cordier, P., and J. C. Doukhan (1991), Water speciation in quartz: A near infrared study, *Am. Mineral.*, *76*(3-4), 361–369.

Cordier, P., and J. C. Doukhan (1989), Water solubility in quartz and its influence on ductility, *Eur. J. Mineral.*, *1*(2), 221–238.

Cordier, P., B. Boulogne, and J. C. Doukhan (1988), Water precipitation and diffusion in wet quartz and wet berlinite $AlPO_4$, *Bull. Mineral.*, *111*(2), 113–137.

Cordier, P., J. C. Doukhan, and C. Ramboz (1994), Influence of dislocations on water leakage from fluid inclusions in quartz: A quantitative reappraisal, *Eur. J. Mineral.*, *6*(6), 745–752.

Darot, M., Y. Gueguen, Z. Bencheman, and R. Gaboriaud (1985), Ductile-brittle transition investigated by micro-indentation: Results for quartz and olivine, *Phys. Earth Planet. Int.*, *40*, 180–186.

den Brok, B., J. Meinecke, and K. Roeller (1994), Fourier transform IR-determination of intragranular water content in quartzites experimentally deformed with and without added water in the ductile deformation field, *J. Geophys. Res.*, *99*, 19,821–19,828, doi:10.1029/94JB01473.

den Brok, S. W. J., and C. J. Spiers (1991), Experimental evidence for water weakening of quartzite by microcracking plus solution-precipitation creep, *J. Geol. Soc. London*, *148*, 541–548.

Diamond, L. W., A. Tarantola, and H. Stünitz (2010), Modification of fluid inclusions in quartz by deviatoric stress I: Experimentally induced changes in inclusion shapes and microstructures, *Contrib. Mineral. Petrol.*, *160*(6), 825–843.

Dodd, D. M., and D. B. Fraser (1965), The 3000–3900 cm^{-1} absorption bands and anelasticity in crystalline α-quartz, *J. Phys. Chem. Solids*, *26*(4), 673–686.

Doppler, G., and R. J. Bakker (2014), The influence of the α-β phase transition of quartz on fluid inclusions during re-equilibration experiments, *Lithos*, *198-199*, 14–23.

Doukhan, J. C. (1995), Lattice defects and mechanical behaviour of quartz SiO_2, *J. Phys. III*, *5*(11), 1809–1832.

Doukhan, J. C., and L. Trépied (1985), Plastic deformation of quartz single crystals, *Bull. Mineral.*, *108*(1), 97–123.

Drury, M. R. (1991), Hydration-induced climb dissociation of dislocations in naturally deformed mantle olivine, *Phys. Chem. Miner.*, *18*(2), 106–116.

Evans, B., and D. L. Kohlstedt (1995), Rheology of rocks, in *Rock Physics and Phase Relations: A Handbook of Physical Constants*, edited by T. J. Ahrens, pp. 148–165, AGU Publ., Washington, D. C., doi:10.1029/RF003p0148.

Farver, J. R., and R. A. Yund (1991), Oxygen diffusion in quartz: Dependence on temperature and water fugacity, *Chem. Geol.*, *90*(1), 55–70.

Fitz Gerald, J. D., J. N. Boland, A. C. McLaren, A. Ord, and B. E. Hobbs (1991), Microstructures in water-weakened single crystals of quartz, *J. Geophys. Res.*, *96*, 2139–2155, doi:10.1029/90JB02190.

Frondel, C. (1982), Structural hydroxyl in chalcedony (type B quartz), *Am. Mineral.*, *67*, 1248–1257.

Gerretsen, J., M. S. Paterson, and A. C. McLaren (1989), The uptake and solubility of water in quartz at elevated pressure and temperature, *Phys. Chem. Miner.*, *16*(4), 334–342.

Gleason, G. C., and S. De Sisto (2008), A natural example of crystal-plastic deformation enhancing the incorporation of water into quartz, *Tectonophysics*, *446*(1), 16–30.

Goodier, J. N. (1933), Concentration of stress around spherical and cylindrical inclusions and flaws, *Trans. ASME*, *55*(APM-55-7), 39–44.

Graetsch, H., O. W. Floerke, and G. Miehe (1985), The nature of water in chalcedony and opal-C from Brazilian agate geodes, *Phys. Chem. Miner.*, *12*(5), 300–306.

Graetsch, H., O. W. Floerke, and G. Miehe (1987), Structural defects in microcrystalline silica, *Phys. Chem. Miner.*, *14*(3), 249–257.

Griggs, D. (1967), Hydrolytic weakening of quartz and other silicates, *Geophys. J. Int.*, *14*, 19–31.

Griggs, D. (1974), A model of hydrolytic weakening in quartz, *J. Geophys. Res.*, *79*, 1653–1661, doi:10.1029/JB079i011p01653.

Griggs, D. T., and J. D. Blacic (1965), Quartz: Anomalous weakness of synthetic crystals, *Science*, *147*(3655), 292–295.

Halliburton, L. E., N. Koumvakalis, M. Markes, and J. Martin (1981), Radiation effects in crystalline SiO_2: The role of aluminum, *J. Appl. Phys.*, *52*, 3565–3574.

Heard, H. C., and N. L. Carter (1968), Experimentally induced "natural" intragranular flow in quartz and quartzite, *Am. J. Sci.*, *266*(1), 1–42.

Heilbronner, R., and S. Barrett (2013), *Image Analysis in Earth Sciences: Microstructures and Textures of Earth Materials*, vol. 129, 455 pp., Springer, Heidelberg, New York.

Heilbronner, R., and J. Tullis (2002), The effect of static annealing on microstructures and crystallographic preferred orientations of quartzites experimentally deformed in axial compression and shear, *Geol. Soc. London, Spec. Publ.*, *200*(1), 191–218.

Hirth, G., and J. Tullis (1992), Dislocation creep regimes in quartz aggregates, *J. Struct. Geol.*, *14*(2), 145–159.

Hirth, G., and J. Tullis (1994), The brittle-plastic transition in experimentally deformed quartz aggregates, *J. Geophys. Res.*, *99*, 11,731–11,747, doi:10.1029/93JB02873.

Hirth, G., C. Teyssier, and J. W. Dunlap (2001), An evaluation of quartzite flow laws based on comparisons between experimentally and naturally deformed rocks, *Int. J. Earth Sci.*, *90*(1), 77–87.

Holyoke, C. W., and A. K. Kronenberg (2010), Accurate differential stress measurement using the molten salt cell and solid salt assemblies in the Griggs apparatus with applications to strength, piezometers and rheology, *Tectonophysics*, *494*(1), 17–31.

Holyoke, C. W., and A. K. Kronenberg (2013), Reversible water weakening of quartz, *Earth Planet. Sci. Lett.*, *374*, 185–190.

Ito, Y., and S. Nakashima (2002), Water distribution in low-grade siliceous metamorphic rocks by micro-FTIR and its relation to grain size: a case from the Kanto Mountain region, Japan, *Chem. Geol.*, *189*(1), 1–18.

Karampelas, S., E. Fritsch, T. Zorba, K. M. Paraskevopoulos, and S. Sklavounos (2005), Distinguishing natural from synthetic amethyst: The presence and shape of the 3595 cm^{-1} peak, *Mineral. Petrol.*, *85*(1-2), 45–52.

Kats, A., Y. Haven, and J. M. Stevels (1962), Hydroxyl groups in α-quartz, *Phys. Chem. Glasses*, *3*(3), 69–75.

Kekulawala, K. R. S. S., M. S. Paterson, and J. N. Boland (1981), An experimental study of the role of water in quartz deformation, in *Mechanical Behavior Crustal Rocks: The Handin Volume*, Geophys. Monograph, vol. 24, edited by N. L. Carter et al., pp. 49–60, AGU Publ., Washington, D. C., doi:10.1029/GM024p0049.

Kidder, S., G. Hirth, J. P. Avouac, and W. Behr (2016), The influence of stress history on the grain size and microstructure of experimentally deformed quartzite, *J. Struct. Geol.*, *83*, 194–206.

Kilian, R., R. Heilbronner, C. W. Holyoke III, A. K. Kronenberg, and H. Stünitz (2016), Dislocation creep of dry quartz, *J. Geophys. Res. Atmos.*, *121*, 3278–3299, doi:10.1002/2015JB012771.

Kirby, S. H. (1975), Creep of synthetic α-quartz, PhD thesis, Univ. of California, Los Angeles.

Kohlstedt, D. L., B. Evans, and S. J. Mackwell (1995), Strength of the lithosphere: constraints imposed by laboratory experiments, *J. Geophys. Res.*, *100*, 17,587–17,602, doi:10.1029/95JB01460.

Kopp, O. C., and P. A. Staats (1970), Characterization of RbOH-grown quartz by infrared and mass spectroscopy, *J. Phys. Chem. Solids*, *31*(11), 2469–2476.

Kronenberg, A. K. (1994), Hydrogen speciation and chemical weakening of quartz, *Rev. Mineral. Geochem.*, *29*(1), 123–176.

Kronenberg, A. K., and J. Tullis (1984), Flow strengths of quartz aggregates: Grain size and pressure effects due to hydrolytic weakening, *J. Geophys. Res.*, *89*, 4281–4297, doi:10.1029/JB089iB06p04281.

Kronenberg, A. K., and G. H. Wolf (1990), Fourier transform infrared spectroscopy determinations of intragranular water content in quartz-bearing rocks: Implications for hydrolytic weakening in the laboratory and within the Earth, *Tectonophysics*, *172*(3), 255–271.

Kronenberg, A. K., S. H. Kirby, R. D. Aines, and G. R. Rossman (1986), Solubility and diffusional uptake of hydrogen in quartz at high water pressures: Implications for hydrolytic weakening, *J. Geophys. Res.*, *91*, 12,723–12,741, doi:10.1029/JB091iB12p12723.

Kronenberg, A. K., P. Segall, and G.H. Wolf (1990) Hydrolytic weakening and penetrative deformation within a natural shear zone, in *The Brittle-Ductile Transition in Rocks: The Heard Volume*, Geophys. Monog., vol. 56, edited by A. G. Duba et al., pp. 21–36, AGU Publ., Washington, D. C.

Kronenberg, A. K., W. M. Lamb, Z. Luo, and L. A. Neal (2001), Redistribution of water during deformation of milky quartz, *Abstr. AGU Fall meeting* T21C-06.

Libowitzky, E., and G. R. Rossman (1997), An IR absorption calibration for water in minerals, *Am. Mineral.*, *82*(11), 1111–1115.

Linker, M. F., and S. H. Kirby (1981), Anisotropy in the rheology of hydrolytically weakened synthetic quartz crystals, in *Mechanical Behavior Crustal Rocks: The Handin Volume*, Geophys. Monograph, vol. 24, edited by N. L. Carter et al., pp. 29–48, AGU Publ., Washington, D. C.

Mainprice, D. H., and M. S. Paterson (1984), Experimental studies of the role of water in the plasticity of quartzites, *J. Geophys. Res.*, *89*, 4257–4269, doi:10.1029/JB089iB06p04257.

McLaren, A. C. (1991), *Transmission Electron Microscopy of Minerals and Rocks, Cambridge Topics in Mineral Phys. Chem.*, vol. 2, 387 pp., Cambridge Univ. Press, Cambridge, U. K.

McLaren, A. C., and P. Phakey (1965), A transmission electron microscope study of amethyst and citrine, *Aust. J. Phys.*, *18*(2), 135–142.

McLaren, A. C., and P. Phakey (1966a), Electron microscope study of Brazil twin boundaries in amethyst quartz, *Phys. Sta. Solidi*, *13*(2), 413–422.

McLaren, A. C., and P. Phakey (1966b), Transmission electron microscope study of bubbles and dislocations in amethyst and citrine quartz, *Aust. J. Phys.*, *19*, 19–24.

McLaren, A. C., and D. Pitkethly (1982), The twinning microstructure and growth of amethyst quartz, *Phys. Chem. Miner.*, *8*(3), 128–135.

McLaren, A. C., R. G. Turner, J. N. Boland, and B. E. Hobbs (1970), Dislocation structure of the deformation lamellae in synthetic quartz: A study by electron and optical microscopy, *Contrib. Mineral. Petrol.*, *29*(2), 104–115.

McLaren, A. C., R. F. Cook, S. T. Hyde, and R. C. Tobin (1983), The mechanisms of the formation and growth of water bubbles and associated dislocation loops in synthetic quartz, *Phys. Chem. Miner.*, *9*(2), 79–94.

McLaren, A. C., J. D. Fitz Gerald, and J. Gerretsen (1989), Dislocation nucleation and multiplication in synthetic quartz: Relevance to water weakening, *Phys. Chem. Miner.*, *16*(5), 465–482.

Mei, S., and D. L. Kohlstedt (2000a), Influence of water on plastic deformation of olivine aggregates: 1. Diffusion creep regime, *J. Geophys. Res.*, *105*, 21,457–21,469, doi:10.1029/2000JB900179.

Mei, S., and D. L. Kohlstedt (2000b), Influence of water on plastic deformation of olivine aggregates: 2. Dislocation creep regime, *J. Geophys. Res.*, *105*, 21,471–21,481, doi:10.1029/2000JB900180.

Menegon, L., P. Nasipuri, H. Stünitz, H. Behrens, and E. Ravna (2011), Dry and strong quartz during melt-assisted deformation in the lower crust, *J. Geophys. Res.*, *116*, B10410, doi:10.1029/2011JB008371.

Miehe, G., H. Graetsch, and O. W. Flörke (1984), Crystal structure and growth fabric of length-fast chalcedony, *Phys. Chem. Miner.*, *10*(5), 197–199.

Morrison-Smith, D. J., M. S. Paterson, and B. E. Hobbs (1976), An electron microscope study of plastic deformation in single crystals of synthetic quartz, *Tectonophysics*, *33*(1), 43–79.

Muto, J., G. Hirth, R. Heilbronner, and J. Tullis (2011), Plastic anisotropy and fabric evolution in sheared and recrystallized quartz single crystals, *J. Geophys. Res.*, *116*, B02206, doi:10.1029/2010JB007891.

Nakashima, S., H. Matayoshi, T. Yuko, K. Michibayashi, T. Masuda, N. Kuroki, H. Yamagishi, Y. Ito, and A. Nakamura (1995), Infrared microspectroscopy analysis of water distribution in deformed and metamorphosed rocks, *Tectonophysics*, *245*(3), 263–276.

Niimi, N., N. Aikawa, and K. Shinoda (1999), The infrared absorption band at 3596 cm^{-1} of the recrystallized quartz from Mt. Takamiyama, southwest Japan, *Mineral. Mag.*, *63*(5), 693–701.

Pankrath, R. (1991), Polarized IR spectra of synthetic smoky quartz, *Phys. Chem. Miner.*, *17*(8), 681–689.

Paterson, M. S. (1982), The determination of hydroxyl by infrared absorption in quartz, silicate glasses, and similar materials, *Bull. Mineral.*, *105*, 20–29.

Paterson, M. S. (1986), The thermodynamics of water in quartz, *Phys. Chem. Miner.*, *13*(4), 245–255.

Paterson, M. S. (1989), The interaction of water with quartz and its influence in dislocation flow: An overview, in *Rheology of Solids and of the Earth*, edited by S. Karato and M. Toriumi, pp. 107–142, Oxford Univ. Press, Oxford.

Paterson, M. S. (2013), *Materials Science for Structural Geology*, 246 pp., Springer, Heidelberg, New York.

Pec, M., H. Stünitz, R. Heilbronner, and M. Drury (2016), Semi-brittle flow of granitoid fault rocks in experiments at mid-crustal conditions, *J. Geophys. Res. Atmos.*, *121*, 1677–1705, doi:10.1002/2015JB012513.

Poirier, J. P. (1985), *Creep of Crystals: High-Temperature Deformation Processes in Metals, Ceramics and Minerals*, 260 pp., Cambridge Univ. Press, Cambridge, U. K.

Post, A. D., J. Tullis, and R. A. Yund (1996), Effects of chemical environment on dislocation creep of quartzite, *J. Geophys. Res.*, *101*, 22,143–22,155, doi:10.1029/96JB01926.

Prasad, P. S. R., K. Shiva Prasad, and N. K. Thakur (2006), FTIR signatures of type-II clathrates of carbon dioxide in natural quartz veins, *Curr. Sci.*, *90*(11), 1544–1547.

Rovetta, M. R. (1989), Experimental and spectroscopic constraints on the solubility of hydroxyl in quartz, *Phys. Earth Planet. Inter.*, *55*(3), 326–334.

Rovetta, M. R., J. R. Holloway, and J. D. Blacic (1986), Solubility of hydroxyl in natural quartz annealed in water at 900 C and 1.5 GPa, *Geophys. Res. Lett.*, *13*, 145–148, doi:10.1029/GL013i002p00145.

Smith, D. L., and B. Evans (1984), Diffusional crack healing in quartz, *J. Geophys. Res.*, *89*, 4125–4135, doi:10.1029/JB089iB06p04125.

Stalder, R., and J. Konzett (2012), OH defects in quartz in the system quartz–albite–water and granite–water between 5 and 25 kbar, *Phys. Chem. Miner.*, *39*(10), 817–827.

Sterner, S. M., D. L. Hall, and H. Keppler (1995), Compositional re-equilibration of fluid inclusions in quartz, *Contrib. Mineral. Petrol.*, *119*(1), 1–15.

Stipp, M., H. Stünitz, R. Heilbronner, and S. M. Schmid (2002a), Dynamic recrystallization of quartz: Correlation between natural and experimental conditions, in *Deformation Mechanisms, Rheology and Tectonics: Current Status and Future Perspectives.*, edited by S. de Meer et al., *Geol. Soc. London Spec. Publ.*, *200*, 171–190.

Stipp, M., H. Stünitz, R. Heilbronner, and S. M. Schmid (2002b), The eastern Tonale fault zone: A "natural laboratory" for crystal plastic deformation of quartz over a temperature range from 250–700°C, *J. Struct. Geol.*, *24*, 1861–1884.

Stipp, M., J. Tullis, and H. Behrens (2006), Effect of water on the dislocation creep microstructure and flow stress of quartz and implications for the recrystallized grain size piezometer, *J. Geophys. Res.*, *111*, B04201, 1–19, doi:10.1029/2005JB003852.

Stünitz, H., J. D. Fitz Gerald, and J. Tullis (2003), Dislocation generation, slip systems, and dynamic recrystallization in experimentally deformed plagioclase single crystals, *Tectonophysics*, *372*(3), 215–233.

Subramaniam, B., L. E. Halliburton, and J. J. Martin (1984), Radiation effects in crystalline SiO_2: Infrared absorption from OH-related defects, *J. Phys. Chem. Solids*, *45*(5), 575–579.

Tarantola, A., L. W. Diamond, and H. Stünitz (2010), Modification of fluid inclusions in quartz by deviatoric stress I: Experimentally induced changes in inclusion shapes and microstructures, *Contrib. Mineral. Petrol.*, *160*(6), 825–843.

Tarantola, A., L. W. Diamond, H. Stünitz, A. Thust, and M. Pec (2012), Modification of fluid inclusions in quartz by deviatoric stress. III: Influence of principal stresses on inclusion density and orientation, *Contrib. Mineral. Petrol.*, *164*(3), 537–550.

Trépied, L., J. C. Doukhan, and J. Paquet (1980), Subgrain boundaries in quartz theoretical analysis and microscopic observations, *Phys. Chem. Miner.*, *5*(3), 201–218.

Trepmann, C. A., and B. Stöckhert (2013), Short wavelength undulatory extinction in quartz recording coseismic deformation in the middle crust-an experimental study, *Solid Earth*, *4*, 263–276.

Trepmann, C. A., B. Stöckhert, D. Dorner, R. H. Moghadam, M. Küster, and K. Röller (2007), Simulating coseismic deformation of quartz in the middle crust and fabric evolution during postseismic stress relaxation: An experimental study, *Tectonophysics*, *442*(1), 83–104.

Tullis, J., and R. A. Yund (1989), Hydrolytic weakening of quartz aggregates: The effects of water and pressure on recovery, *Geophys. Res. Lett.*, *16*, 1343–1346, doi:10.1029/GL016i011p01343.

Tullis, J., G. L. Shelton, and R. A. Yund (1979), Pressure dependence of rock stength—Implications for hydrolytic weakening, *Bull. Mineral.*, *102*(2-3), 110–114.

Tullis, T. E., and J. Tullis (1986), Experimental rock deformation techniques, in *Mineral and Rock Deformation: Laboratory Studies. The Paterson Volume*, *Geophys. Monog.*, vol. 36, edited by B. E. Hobbs and H. C. Heard, pp. 297–324, AGU Publ., Washington, D. C., doi: 10.1029/GM036p0297.

Vernooij, M. G. C., K. Kunze, and B. den Brok (2006), Brittle shear zones in experimentally deformed quartz single crystals, *J. Struct. Geol.*, *28*(7), 1292–1306.

Walker, A. M., J. Hermann, A. J. Berry, and H. S. C. O'Neill (2007), Three water sites in upper mantle olivine and the role of titanium in the water weakening mechanism, *J. Geophys. Res.*, *112*, 1–12, doi:10.1029/2006JB004620.

Wanamaker, B. J., T. F. Wong, and B. Evans (1990), Decrepitation and crack healing of fluid inclusions in San Carlos olivine, *J. Geophys. Res.*, *95*, 15,623–15,641, doi:10.1029/JB095iB10p15623.

Wood, D. L. (1960), Infrared absorption of defects in quartz, *J. Phys. Chem. Solids*, *13*(3), 326–336.

Yamagishi, H., S. Nakashima, and Y. Ito (1997), High temperature infrared spectra of hydrous microcrystalline quartz, *Phys. Chem. Miner.*, *24*(1), 66–74.

Zhao, Y. H., S. B. Ginsberg, and D. L. Kohlstedt (2004), Solubility of hydrogen in olivine: Dependence on temperature and iron content, *Contrib. Mineral. Petrol.*, *147*(2), 155–161.